Chapter 5

EQUATORIAL CURRENTS

1 Phenomenology

Tropical circulation is unique because of the vanishing of the Coriolis frequency f at the equator, with

$$f \approx \beta y$$

in the vicinity of the equator at $y = 0$. This is called the *equatorial β-plane approximation*), and it has several dynamical consequences. One is that geostrophic balance is much less reliable *a priori* as a large-scale dynamical approximation, although some of the most important zonal currents approximately remain geostrophic even at the equator (this requires that the meridional pressure gradient vanish there too). Another consequence is that the inviscid, adiabatic conservation of potential vorticity, q, constrains parcel displacements from crossing the equator for any substantial distance, since q must assume the sign of f away from the equator and this sign is different in the different hemispheres. This means that the mean circulation and most long-time parcel displacements are primarily zonal near the equation, but it also focuses our attention on locations (*e.g.,* surface PBL, deep WBC) where mixing processes break the constraint of q conservation. A third consequence is that the equatorial band is an effective zonal waveguide for distinctive, zonally propagating Kelvin, Rossby, Yanai, and gravity wave modes. These waves can support east-west mass adjustment processes, including some essential behaviors for the most important global, coupled climate-variability mode on intermediate time scales, *viz.,* El Niño – Southern Oscillation (ENSO) (Philander, 1990). A fourth consequence is that the "linear" Ekman depth,

$$h_{ek} \approx \sqrt{\boldsymbol{\tau}}/f \to \infty \text{ as } f \to 0\,;$$

i.e., the steady-state boundary-layer depth might reach all the way to the bottom. However, in practice this is prevented mostly by a strong stable density stratification but also by equatorial upwelling and nonlinear boundary-layer dynamics.

In analogy with the mid-latitude definition of the baroclinic deformation radius (*i.e.,* $R = NH/f$) as an important horizontal scale for circulation, eddies, and planetary waves, we can make a scaling estimation for the equatorial deformation radius by replacing f with $\beta y \sim \beta R$, whence

$$R = NH/\beta R \quad \Rightarrow \quad R = \sqrt{NH/\beta}\,. \tag{1}$$

This has a value of $R \approx 200$ km for $\beta = 2 \times 10^{-11}$ m^{-1} s^{-1}, $N = 4 \times 10^{-3}$ s^{-1}, and $H = 250$ m (appropriate to the rather shallow depth of the equatorial pycnocline). This value is substantially larger than typical extra-tropical R values ≤ 50 km. We shall see that this is roughly the meridional

width of the zone in which the equator is distinctly different in its dynamics, as indicated by the Equatorial Undercurrent and the most energetic, zonally propagating equatorial waves.

We have already seen several aspects of the measured Equatorial forcing and circulation in Chaps. 1-3:

- Surface trade winds (Chap. 2, Figs. 2-3)
- Surface equatorial heating (Chap. 2, Figs. 5 and 7) and freshwater flux (Chap. 2, Fig. 9)
- Equatorial divergence of Ekman transport as a result of the sign change in f and the generally easterly trade winds (Chap. 2, Fig. 11)
- Meridional Overturning Circulation (MOC) streamfunction showing equatorial upwelling (Chap. 1, Fig. 5)
- Surface Equatorial Current (Chap. 1, Figs. 2 and 12)
- Sverdrup transport showing the North Equatorial Countercurrent (Chap. 2, Fig. 12; Chap. 3, Fig. 2)
- Meridional sections of T, S, and u showing the strong, shallow pycnocline; the equatorial water-mass boundary in S; and the surface Equatorial Current (EC), Equatorial Undercurrent (EUC), and North Equatorial Countercurrent (NECC) (Chap. 1, Figs. 6, 8, and 9).

Another sketch of the principal equatorial currents is Fig. 1. In particular, it indicates strong upwelling along the eastern boundary near Peru, as well as an advection of cold water there from the South American coast in the Peru (or Humbolt) Current.

2 Mean Zonal Currents

Figures 2-4 show several further views of the mean zonal currents in a meridional plane near the equator. Note the various currents: Equatorial Current (EC), Equatorial Undercurrent (EUC), North Equatorial Countercurrent (NECC), and the deep zonal jets. Also note that the EC and EUC have quite similar structures in (y, z) in all three oceans. Their meridional scale is about the same as estimated above for R. The bulge in the isotherms above and below the EUC is qualitatively consistent with a meridional geostrophic momentum balance for an eastward current with its maximum speed in the pycnocline. The geostrophic balance is valid even as $y \to 0$, since $\partial_y \phi \to 0$ too insofar as the EUC is equatorially symmetric about $y = 0$. Figure 4 shows the Sverdrup transport streamfunction for the Atlantic, indicating clearly the forcing for the NECC due to the wind-curl; however, the EC-EUC structure is not evident in the Sverdrup transport because

they are substantially baroclinic in their structure and have little vertically integrated horizontal transport.

Figures 5-7 show the distribution of dynamic height and isotherms in the equatorial plane: sea level slopes up to the west and the pycnocline slopes down to the west, consistent $\boldsymbol{\nabla}_h \phi \approx 0$ in the abyss. This structure occurs in both the Atlantic and Pacific (as well as in the Indian, not shown here). Notice in Fig. 7 the large variability that occurs for the pycnocline depth, especially in the east; the greatest part of this is associated with either the seasonal cycle or ENSO.

2.1 Equatorial-Plane Currents

The zonal momentum balance in this plane is illustrated in Fig. 8; notice that it occurs without the influence of the Coriolis force, due to small f and $\overline{v}$ near $y = 0$. A very simple form for the momentum balance is

$$\nu_v u_{zz} \ = \ \phi_x \, , \tag{2}$$

for an upper-ocean fluid layer of depth H, with

$$\nu_v u_z \ = \ \frac{1}{\rho_0} \tau^x \ \text{at} \ z \ = \ 0 \, ,$$
$$\nu_v u_z \ = \ 0 \ \text{at} \ z \ = \ -H \, .$$

H is interpreted as the pycnocline depth, and τ^x is the zonal wind stress. The model is unstratified, but implicitly stratification is invoked to limit the circulation to $ze.g., -H$. We assume that the zonal pressure gradient is independent of depth; this is an essentially *ad hoc* assumption, but it is based on general fluid dynamical experience that pressure forces do not vary much on the scale of a boundary layer and the particular idea that mass is pushed in the direction of the wind so that sea level and dynamic height increase in the downwind direction. Thus,

$$\phi_x \ = \ \frac{1}{\rho_0 H} \tau^x ,$$

and for τ^x negative, ϕ_x is also negative. The current profile resulting from these equations is plotted in Fig. 9. It shows that the current is more westward near the surface. If we further add the constraint that

$$\int_{-H}^{0} u \, dz \ = \ 0$$

(consistent with no net zonal transport in the equatorial plane), then the current profile is

$$\begin{aligned} u(z) \ &= \ \frac{H\tau^x}{\rho_0 \nu_v} \left[\frac{1}{2} \left(\frac{z}{H} \right)^2 + \left(\frac{z}{H} \right) + \frac{1}{3} \right] , \\ &\rightarrow \ \frac{1}{3} \frac{H\tau^x}{\rho_0 \nu_v} , \qquad z \rightarrow 0 \, , \\ &\rightarrow \ -\frac{1}{6} \frac{H\tau^x}{\rho_0 \nu_v} , \qquad z \rightarrow -H \, . \end{aligned} \tag{3}$$

This has an eastward current at depth (the EUC) and a westward current near the surface (the EC). Of course, this flow is not inconsistent with a geostrophic balance in the meridional momentum equation,

$$f u \;=\; -\,\phi_y\,,$$

but the y structure of ϕ (and u) is not explicitly considered in this equatorial plane model. Nevertheless, even this simple model represents the primary structure of the equatorial current system.

2.2 3D Linear Model for Equatorial Currents

The simplest 3D theory for the EC-EUC current dynamics comes from a linear, viscous model with uniform density (Gill, 1975):

$$\begin{aligned} -\beta y v &= -\phi_x + [\nu_v u_z]_z - r u \\ \beta y u &= -\phi_y + [\nu_v v_z]_z - r v \\ u_x + v_y + w_z &= 0, \end{aligned} \tag{4}$$

where r is a constant "drag" parameter. (The use of r rather than a horizontal eddy viscosity is made for analytical convenience; see the next subsection for the latter modeling choice.) The boundary conditions in z are $w = 0$ at $z = -H$ and 0, the viscous stress at the top surface is equal to the wind stress τ, and free-slip (zero stress) at the bottom surface, as in the equatorial-plane model. A vertical integral of the curl of (4) and the usual definition of a horizontal transport streamfunction Ψ,

$$H \int u\, dz \;=\; -\,\Psi_y\,, \quad H \int v\, dz \;=\; \Psi_x\,,$$

lead to

$$\rho_0 r(\Psi_{xx} + \Psi_{yy}) + \beta \Psi_x \;=\; \hat{\mathbf{z}} \cdot \boldsymbol{\nabla} \times \boldsymbol{\tau}\,, \tag{5}$$

which has no singular behavior near the equator and no explicit dependence on the pressure gradient force. The corresponding solution for the pressure gradient is determined by

$$H\Phi_x \;=\; \frac{1}{\rho_0}\tau^x, \quad H\Phi_y \;=\; \frac{1}{\rho_0}\tau^y\,, \tag{6}$$

where Φ is depth-averaged geopotential function. If we further assume that the pressure gradient force is depth-independent for $0 \geq z \geq -H$ (again as in the equatorial-plane model), then $\phi = \Phi$.

If we assume that $\boldsymbol{\tau}$ is spatially uniform, then we can take the trivial solution to (5), *viz.,* $\Psi = 0$. Below the surface (turbulent) boundary layer where ν_v is necessary, we can assume that $\nu_v = 0$, so the momentum balance simplifies to

$$\begin{aligned} -\rho_0 \beta y v &= -\frac{\tau^x}{\rho_0 H} - r u \\ \rho_0 \beta y u &= -\frac{\tau^y}{\rho_0 H} - r v \end{aligned} \tag{7}$$

for $-h \geq z \geq -H$ (where $z = -h$ is the bottom of the boundary layer). This is a linear algebraic system for the velocity, whose solution is depth-independent:

$$\begin{aligned} u &= \frac{-r\tau^x - \beta y \tau^y}{H\rho_0(r^2 + \beta^2 y^2)} \\ v &= \frac{-r\tau^y + \beta y \tau^x}{H\rho_0(r^2 + \beta^2 y^2)} \,. \end{aligned} \tag{8}$$

In particular, we see that $u > 0$ when $\tau^x < 0$ and $\tau^y = 0$ (Fig. 10); thus the EUC is a result of the penetration of the zonal wind stress via the zonal pressure gradient into the layer beneath the surface boundary layer where ν_v vanishes. In this situation, $v < 0$ for $y > 0$, and $v > 0$ for $y < 0$; *i.e.,* there is inflow into the EUC from both sides. From the incompressible continuity equation, the associated vertical velocity below the boundary layer is

$$w \;=\; -\frac{1}{\rho_0}\left(\frac{z+H}{H}\right)\frac{\beta(r^2 - \beta^2 y^2)\tau^x + 2r\beta^2 y\tau^y}{(r^2+\beta^2 y^2)^2} \,. \tag{9}$$

For $\tau^x < 0$ and $\tau^y = 0$, this formula implies upward vertical motion in the core of the EUC that increases upward from $w = 0$ and $z = -H$ and downward motion away from the core (Fig. 10).

Within the surface boundary layer, $\nu_v \neq 0$, and all the terms in (4) contribute. We again solve for $u(z)$ and $v(z)$ with specified Φ, stress boundary conditions top and bottom, and the zero-transport constraint, $\int_{-H}^{0} \mathbf{u}_h dz \;=\; 0$. Notice that this surface boundary layer is different from the mid-latitude Ekman layer because its transport is in the direction of the wind stress. The drag parameter r plays an important role in avoiding singular solutions (*e.g.,* in (8)-(9)). This model is an extension of (2) above and is useful for assessing how the currents change if $\tau^y \neq 0$ and how they decay in amplitude as $|y|$ increases away from the equator even though $\boldsymbol{\tau}$ is constant.

2.3 Zonal Boundaries and Nonlinear Equatorial Currents

The preceding models fail near the eastern and western boundaries, where $u = 0$. A slightly more complicated model, which can represent the behavior near these boundaries, comes from replacing $-r\mathbf{u}$ in (4) with $\nu_h \nabla_h^2 \mathbf{u}$. An example of its solution is shown in Fig. 10, assuming $\tau^y = 0$. From this solution we can evaluate the vertically averaged horizontal Reynolds stress, $\overline{uv}(y)$, also shown in Fig. 10. We note that its effect is to accelerate the flow towards the east near the equator and towards the west away from the equator. So it acts to resist the westward wind stress by transporting westward momentum away from the equator. So, a nonlinear EUC model will have a horiozntal Reynolds stress divergence at least partly replace eddy diffusion, consequently with a stronger and sharper meridional EUC profile (Fig. 11). One can similarly show from (8)-(9) or Fig. 10 that the vertical Reynolds stress, $\overline{uw}(z)$, acts to decelerate the EUC in its core and accelerate it on its periphery, as well as to decelerate the EC near the surface. The shape of the real EUC is, therefore, expected to be significantly influenced by these nonlinear advective forces. Pedlosky (1987) is an example of a nonlinear, analytic solution.

2.4 Equatorial Deep Jets

The equatorial deep zonal jets in Fig. 3 are found in all basins, and they have very long zonal and temporal correlation scales. Several theoretical explanations of their occurrence have been put forward, and this is not a settled issue yet. Among the most plausible explanations are centrifugal instability for currents near the equator (where potential vorticity changes sign, a necessary condition for this type of instability) and a large-scale instability associated with short Yanai waves (Sec. 3), in each case with an associated finite-amplitude equilibration process for the deep jets (Hua et al., 1997; d'Orgeville et al., 2006).

2.5 OGCM Equatorial Currents

As a final topic, we consider what it takes for a GCM to calculate the equatorial currents. In a traditionally coarse-gridded GCM, with meridional grid size of several 100 km, the peak current speed in the EUC is too weak by nearly an order of magnitude and the meridional breadth is far too large (*e.g.,* compared to R or Fig. 2). It has been a long-standing practice for modelers interested in equatorial currents to use a non-uniform meridional grid spacing in the tropical region of $|\phi| \leq 10^o$, say. With a grid spacing finer than about 1^o, the EUC structure is much improved. It is equally important, though, to specify the eddy viscosity appropriately. The key conditions are that ν_h be $\mathcal{O}(10^3)$ m^2 s^{-1} with respect to meridional diffusion and that ν_v be $\mathcal{O}(10^{-4})$ m^2 s^{-1} in the stably stratified upper ocean but it must substantially increase on the eastern underside of the EUC where $Ri = N^2/|u_z^2|$ decreases to $\mathcal{O}(1)$ due to large shear underneath the strongest part of the pycnocline. The rationale for an increased ν_v where Ri is small is the onset of Kelvin-Helmoholtz instability and its associated vertical mixing.

A fairly successful EUC simulation is shown in Fig. 12 for an OGCM calculation that has the characteristics just described.

3 Transient Dynamics

The trade winds have a strong seasonal cycle (*e.g.,* Fig. 13), as well as significant intra-seasonal (*e.g.,* the Madden-Julian Oscillation, MJO) and interannual (*e.g.,* ENSO) variability. Consequently, the forced transient response of the circulation is of considerable interest. In this section we describe several transient behaviors.

3.1 Equatorial Waves

Consider a linear, conservative, shallow-water model on the equatorial β-plane, which can also be viewed as governing the (x, y, t) linear dynamics of the nth vertical mode:

$$\begin{aligned} u_t - \beta y v &= -\phi_x \\ v_t + \beta y u &= -\phi_y \\ \phi_t + c^2[u_x + v_y] &= 0. \end{aligned} \tag{10}$$

Here c is the gravity wave speed of the shallow fluid layer, $c = \sqrt{g'H}$ or $c = \sqrt{gH'}$, depending upon whether one prefers to characterize the oceanic pycnocline stratification effect as having a "reduced gravity" (g') or an "equivalent depth" (H'). Or, it can be viewed as the gravity wave speed c_n that comes from solving the vertical eigenvalue problem associated with the vertical stratification. For the ocean, $c_1 \approx 3$ m s^{-1} in the equatorial Pacific.

After various manipulations (10) can be transformed into a single-variable PDE for v:

$$\frac{\partial}{\partial t}\left[c_n^{-2}\left(\frac{\partial^2 v}{\partial t^2} + \beta^2 y^2 v\right) - \nabla_h^2 v\right] - \beta\frac{\partial v}{\partial x} = 0\,. \tag{11}$$

This has eigensolutions of the form

$$v = D_m[\sqrt{2\beta/c_n}\,y]\cos(kx - \omega t)\,. \tag{12}$$

Here D_m is the parabolic cylinder function, related to the Hermite polynomial function H_m as follows:

$$D_m[\alpha] = 2^{-m/2}H_m[\alpha/\sqrt{2}]e^{-\alpha^2}\,. \tag{13}$$

D_m both oscillates through H_m and decays at large distance through the exponential factor. Its structure can be either even or odd symmetric relative to the equator, depending upon the order index m. Thus, the eigensolutions are equatorially trapped on a scale

$$\Delta y = \sqrt{c_n/2\beta} \sim [g'H]^{1/4}\beta^{-1/2}$$

(*cf.,* R in eqn. (1)). The band with $|y| < \Delta y$ is sometimes referred to as the *equatorial wave guide*. The eigenfrequencies ω_{nm} associated with (12) are the solutions of the cubic equation,

$$\left(\frac{\omega}{c_n}\right)^2 - k^2 - \frac{\beta k}{\omega} = (2m+1)\frac{\beta}{c_n}\,, \tag{14}$$

plus one more mode (the Kelvin mode) with

$$\omega_n^K = c_n k \tag{15}$$

and $v = 0$. The solutions to (14)-(15) are plotted in Fig. 14, in a non-dimensional form that makes them applicable to all n values (refer to the caption). They are of four distinct types: the Kelvin

mode, the family of westward-propagating Rossby modes (lower left, for $m = 1, 2, ...$), the family of gravity modes (upper, for $m = 1, 2, ...$), and the so-called "mixed Rossby-gravity" or "Yanai" mode that separates these other types ($m = 0$).

A planetary wave analysis of interannual variability observed in the equatorial Pacific is shown in Fig. 15. It shows how both Rossby and Kelvin waves are generated and propagate along the equation. Their amplitude is especially large during 1997, which is an ENOS year. Also notice their reflection patterns off the eastern or western boundaries, where a Kelvin wave reflects as a Ross by wave or *vice versa*.

Figures 16-17 show two impulsively forced solutions in which the equatorial wave dynamics are dominant in the oceanic adjustment:

- The sudden onset of a spatially localized, zonal wind stress for a single fluid layer (Fig. 16). This is sometimes taken as a canonical event for the onset of ENSO, resulting from a relaxation of the Trade Winds (or a *westerly wind burst*) in the western and/or central Pacific regions. Note the leakage of mass from the equatorial waveguide through poleward propagating coastal Kelvin waves at the eastern boundary; their dynamics will be further discussed in Chap. 8.

- The spin-up of the EUC from rest in a multi-layer (multi-mode) model, where the zonally uniform zonal wind-stress divergence is applied uniformly in depth over a boundary layer of thickness 150 m (Fig. 17). The transient phases of this spin-up are sometimes called the Wyrtki-Yoshida Jet, and it is considered relevant to the seasonal reversal of the zonal winds at the equator in the Indian Ocean.

These two solutions illustrate how the tropical ocean adjusts to variable wind.

3.2 Tropical Instability Waves

The EUC is generally believed to be fairly stable to mesoscale perturbations, but not necessarily to Kelvin-Helmholtz instabilities associated with the large vertical shears above and below the core. (Baroclinic instability, sustained by vertical shear, disappears as $f \to 0$.) However, the horizontal shear between the EC and the NECC is observed to be sometimes barotropically unstable (*e.g.,* it can satisfy the Rayleigh necessary condition for instability, $\beta + u_{yy}$ changing sign in y), and the resulting eddy motions are often called *Tropical Instability Waves* (TIWs). They are evident as cusps on the near-equatorial meridional gradient of SST (Fig. 18), and they propagate westward (Fig. 19). Although their existence and propagation is often rationalized by linear wave theory, their speed is quite substantial and is more suggestive of a vortex flow — with material properties trapped within its core as it propagates — than a wave just passing through the region (Fig. 20).

3.3 ENSO

ENSO is illustrated in Figs. 21 and 22. This phenomenon comprises one of the strongest signals in the otherwise rather noisy regime of interannual intrinsic climate variability, and the atmospheric manifestations approach the spatial scale of the globe. It is generally understood that ENSO arises through dynamical coupling of the upper tropical ocean with the local tropical atmosphere. The important oceanic ingredients are Kelvin and Rossby wave adjustments to changes in the wind stress, which change the pattern of the thermocline depth and currents, which in turn produces anomalous thermal advection (*i.e.,* $\mathbf{u}' \cdot \boldsymbol{\nabla}\overline{T}$) and modifies the SST. The primary atmospheric ingredient is a quasi-stationary wind response to a SST anomaly. Together these relations close the feedback loops for ocean-atmosphere co-evolution. This topic has an extensive theoretical and observational literature (Philander, 1990; Neelin et al., 1998), so it will not be discussed further here.

4 Eulerian and Eddy-Induced Meridional Overturning

The upper tropical oceans comprise the core of the global Warm Water Sphere (Wüst, 1949). This regime is strongly stably stratified in potential density (Fig. 23a), primarily due to the dominance of solar heating, and it has strong zonal currents (Fig. 23b). It contains some of the globally most important meridional and vertical oceanic heat fluxes that must pass through its bounding isopycnal $\sim$ isothermal surfaces (McWilliams et al., 1996). Inspired by recent measurements of the eddy-induced meridional overturning circulations (MOC) v^* in the tropical North Pacific Ocean by Roemmich and Gilson (2001) (among the few places in the ocean where this quantity has been measured), we analyze an OGCM for its Eulerian and eddy-induced MOC in the tropics (Figs. 23c,d and 24). The model representation for the eddy-induced circulation is the parameterization by Gent and McWilliams (1990). The eddy-induced circulation is similar in all tropical basins. It has a strength of about 10% of the Eulerian (Ekman) circulation, and its contribution to the meridional heat flux is a similar fraction (Fig. 27). The pattern of the meridional streamfunction is one of double cells in the vertical and antisymmetry about the equator. Near the equator there is downwelling above the undercurrent and upwelling below, with the return circulations closed within the upper 250 m and $\pm 5^o$ of latitude. Away from the equator in each basin, there are overturning cells with flow in the opposite direction to those nearest the equator, and they reach deeper into and through the main pycnocline as well as poleward into the subtropics. Similar to the wind-driven Eulerian MOC, the seasonal cycle in the eddy-induced circulation has a magnitude comparable to the time-mean circulation, although for an entirely different dynamical reason than associated with seasonal changes in the buoyancy field that is diabatically forced from the surface (Fig. 26). The simulation also has a circulation anomaly during the 1997-98 ENSO event that nearly cancels the counter-rotating, eddy-induced cells near the equator and surface. The rather good agreement between the measurements and the model solution (Fig. 25) gives support to the theory underlying the parameterization of eddy-induced circulation, and it indicates that the

associated eddy transport coefficients are larger in the tropics (*i.e.,* $\sim\ 2\times 10^3$ m^{2}s^{-1}) than in middle and high latitudes, consistent with measured float dispersion rates (*cf.,* Chap. 1, Fig. 14) (Krauss and Böning, 1987; Sundermeyer and Price, 1998; Bauer et al., 1998). A simple rationalization of larger lateral eddy diffusivity in the tropics comes from the mixing-length estimate,

$$\kappa\ \sim\ V'L'\,,$$

where V' and L' are characteristic eddy velocity and length scales. If, as often, the horizontal length scale L' is approximately the same as the baroclinic deformation radius R, a tropical region with similar eddy energy compared to an extra-tropical one (*i.e.,* similar V') will have larger $\kappa \sim V'R$ because the tropical R is larger.

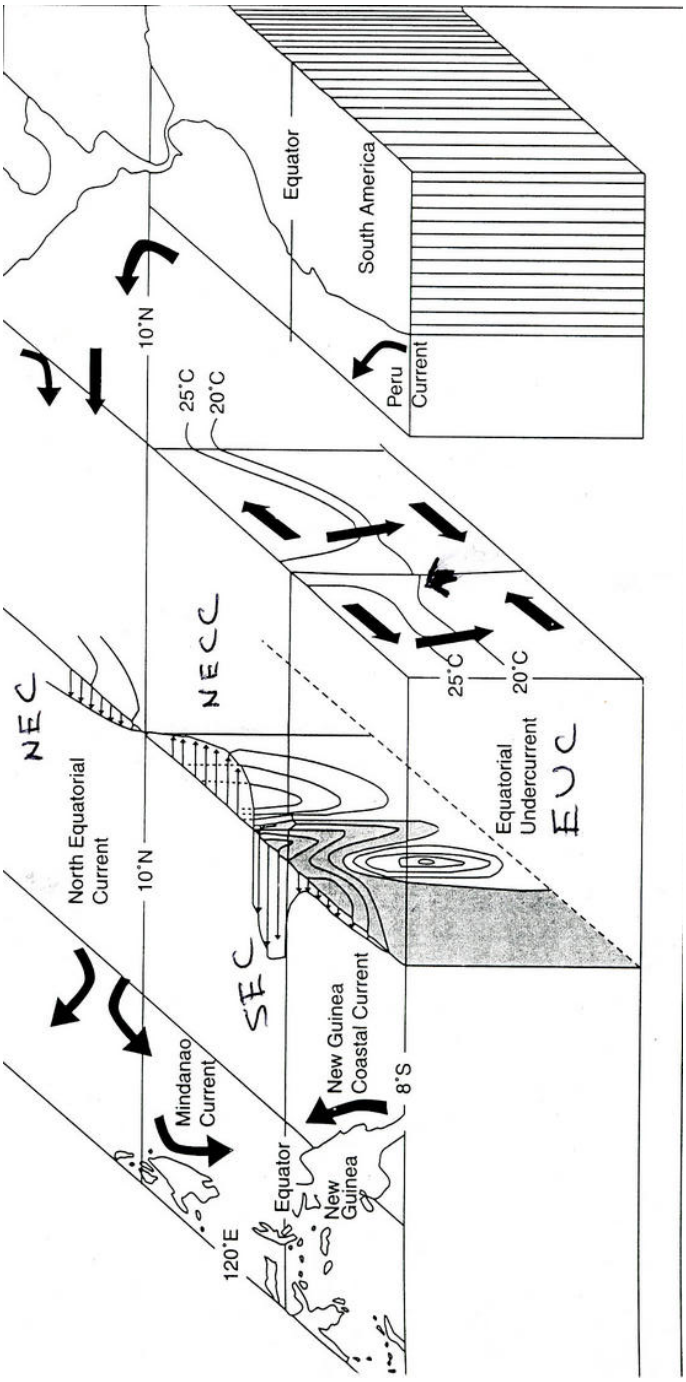

Figure 1: Schematic of flow patterns in the equatorial Pacific Ocean. Adapted from Philander (1990).

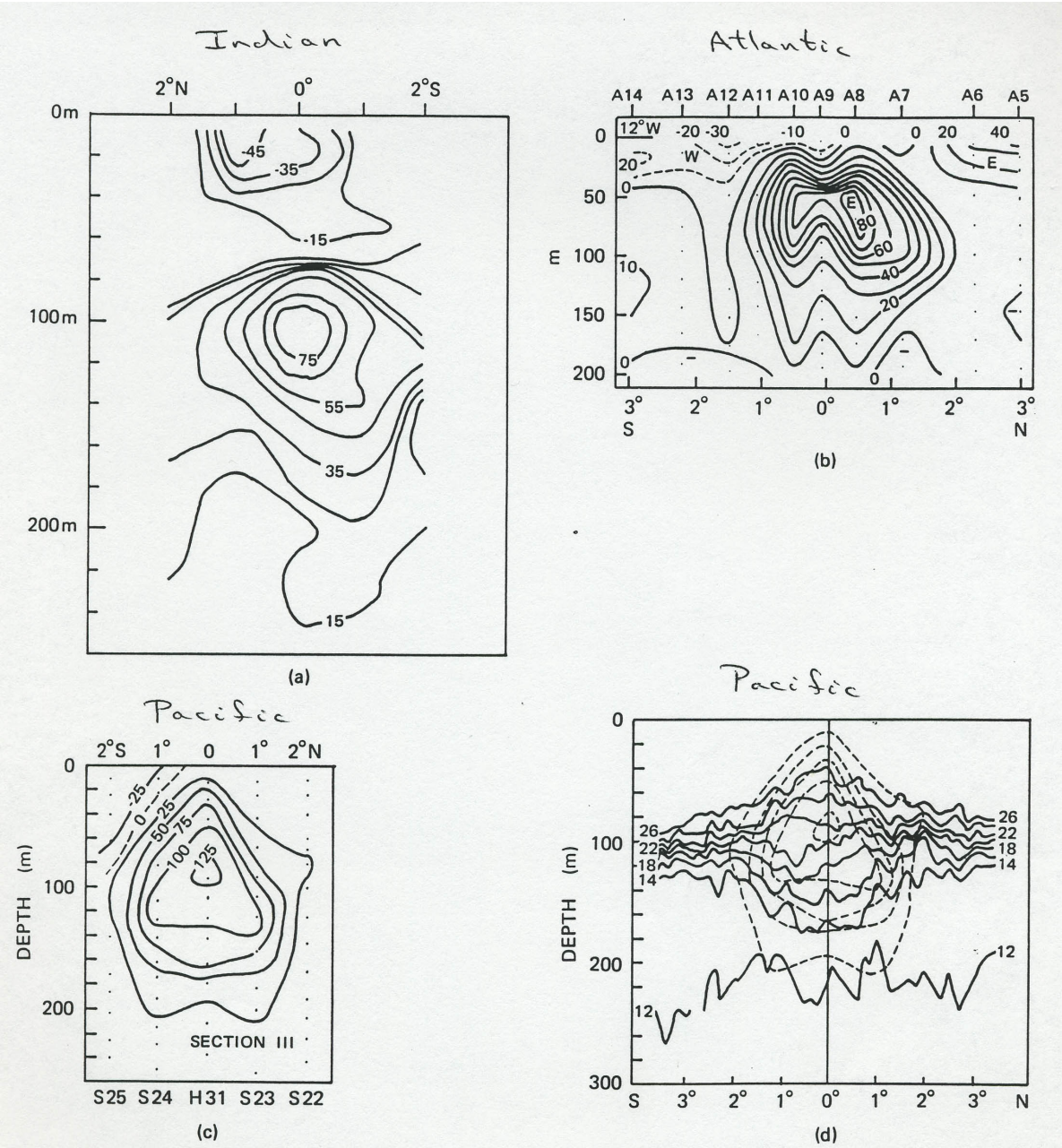

Figure 2: Upper-ocean, equatorial, meridional sections of zonal velocity in the Indian, Atlantic, and Pacific Oceans (Taft, 1967; Sturm and Voigt, 1966; Knauss, 1960).

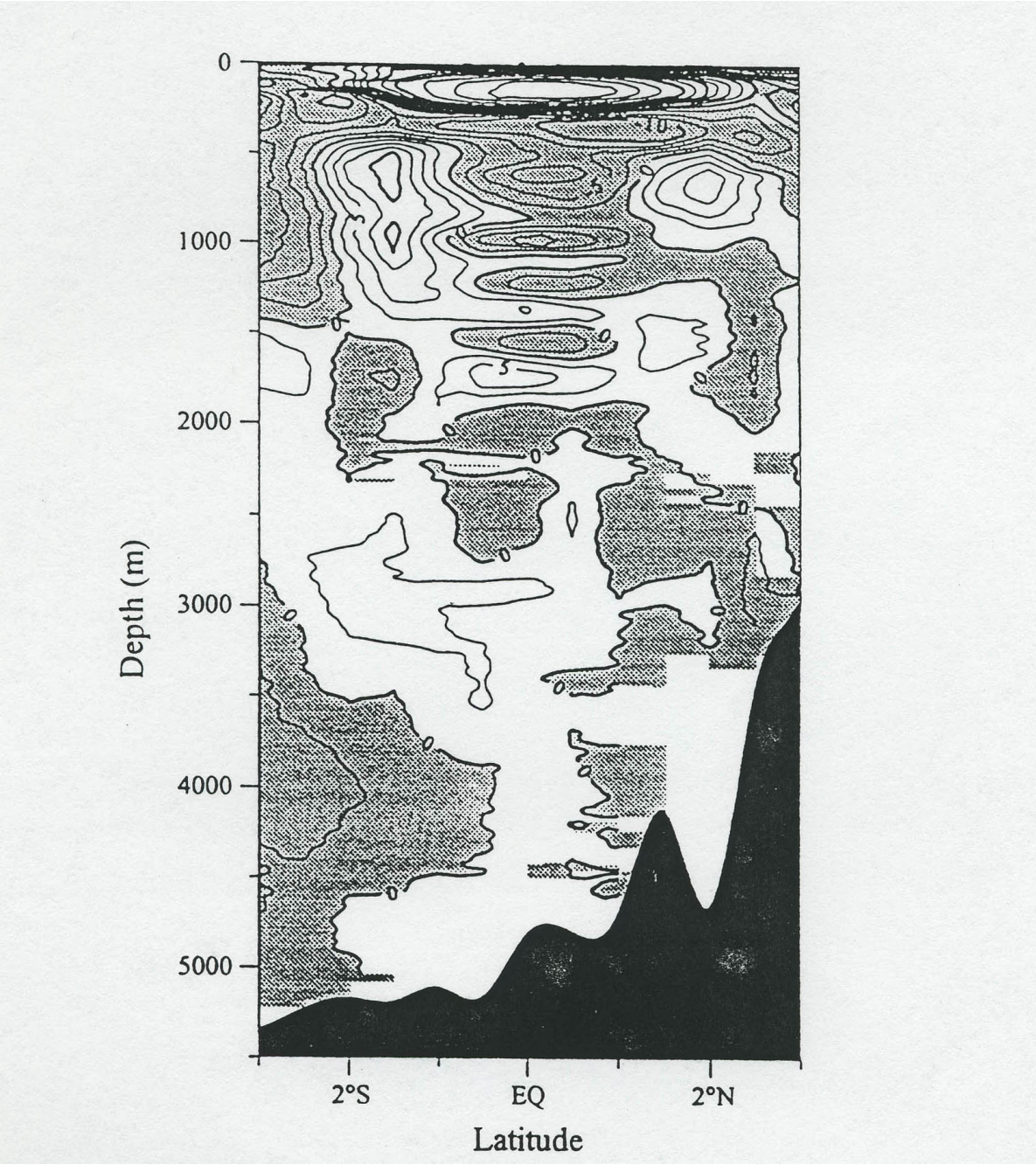

Figure 3: Full-depth, equatorial, meridional section of zonal velocity in the Pacific basin (Firing, 1987).

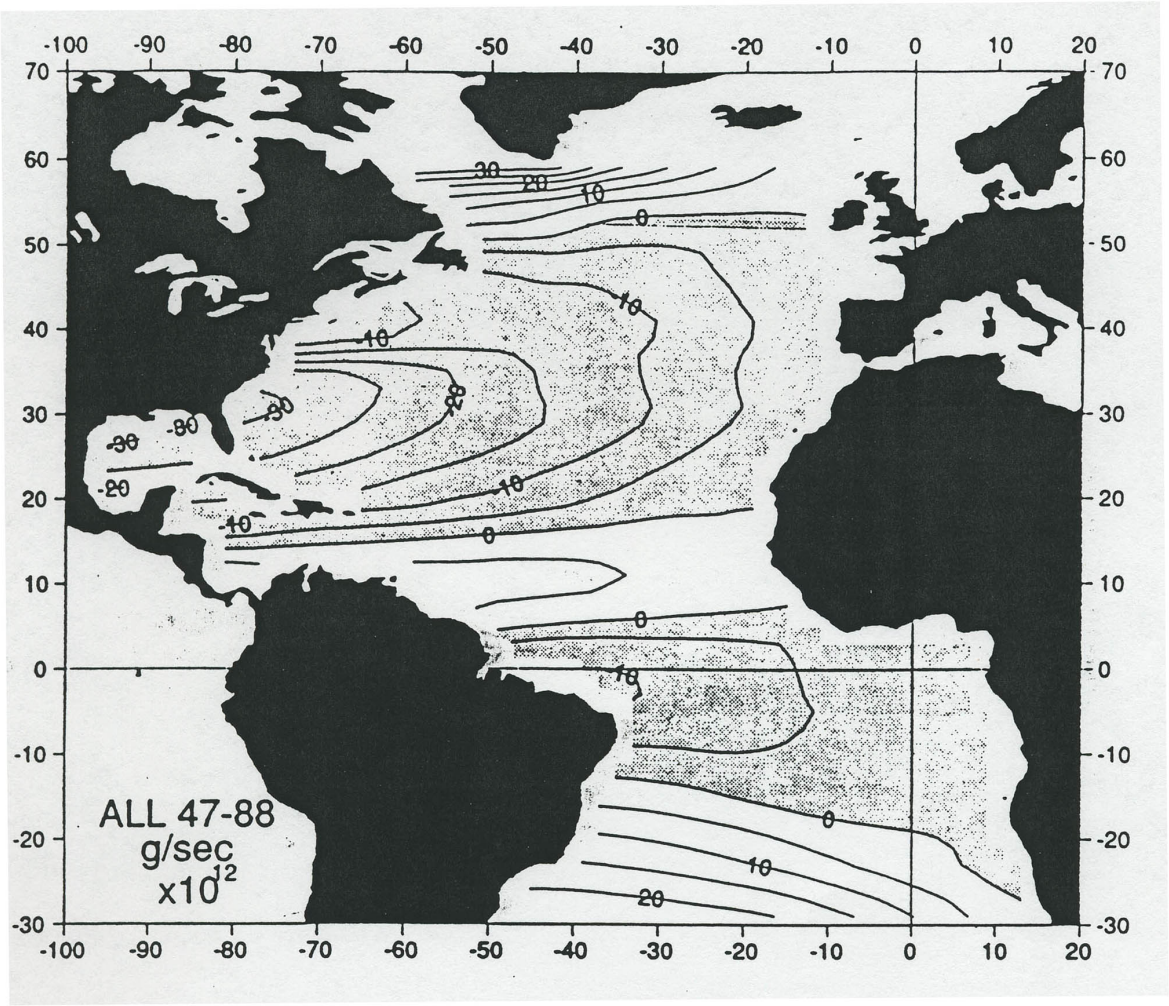

Figure 4: Annual mean Sverdrup transport streamfunction in the Atlantic (Mayer and Weisberg, 1993).

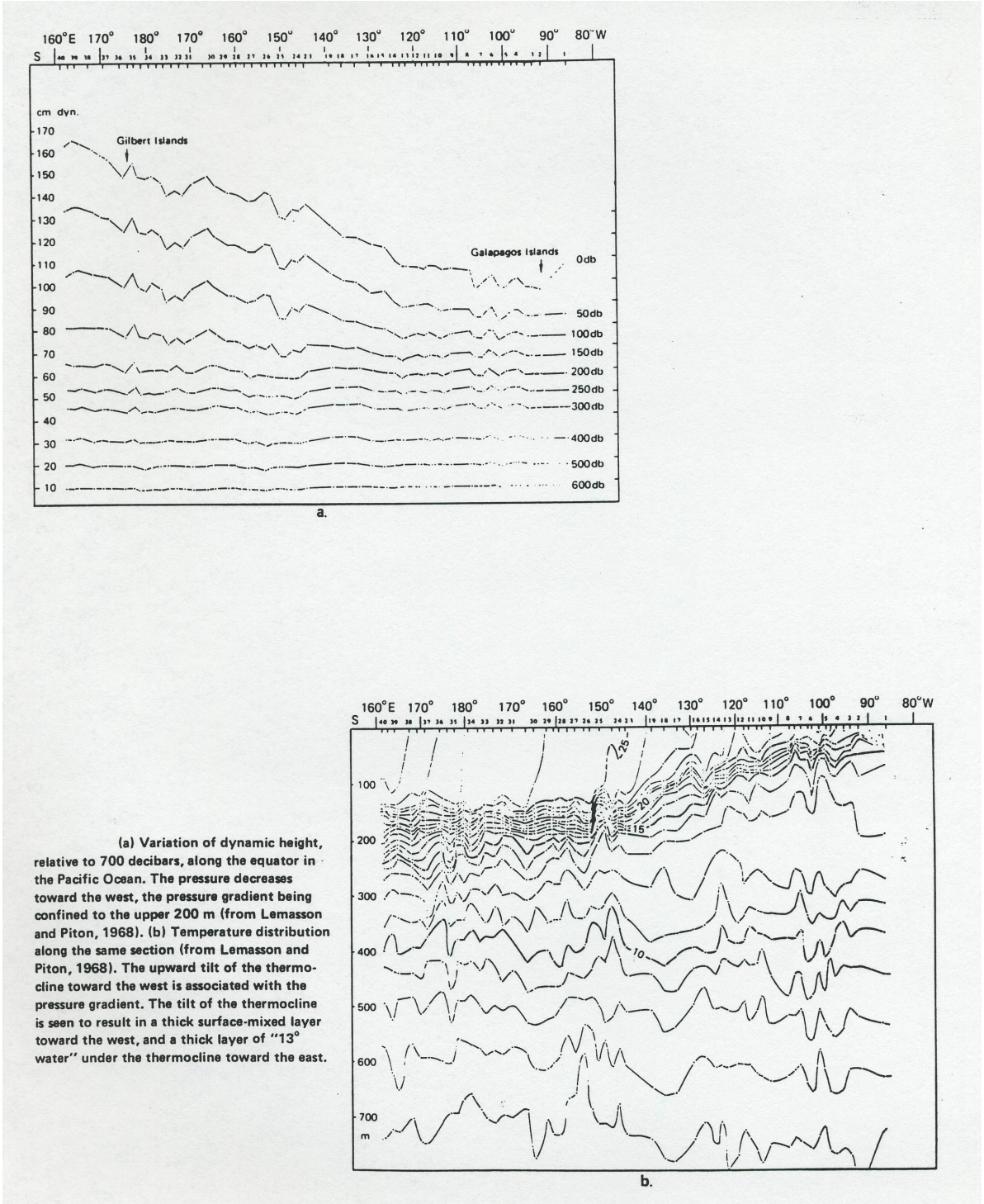

(a) Variation of dynamic height, relative to 700 decibars, along the equator in the Pacific Ocean. The pressure decreases toward the west, the pressure gradient being confined to the upper 200 m (from Lemasson and Piton, 1968). (b) Temperature distribution along the same section (from Lemasson and Piton, 1968). The upward tilt of the thermocline toward the west is associated with the pressure gradient. The tilt of the thermocline is seen to result in a thick surface-mixed layer toward the west, and a thick layer of "13° water" under the thermocline toward the east.

Figure 5: Upper-ocean, equatorial, zonal sections of dynamic height and T in the Pacific (Lemasson and Piton, 1968).

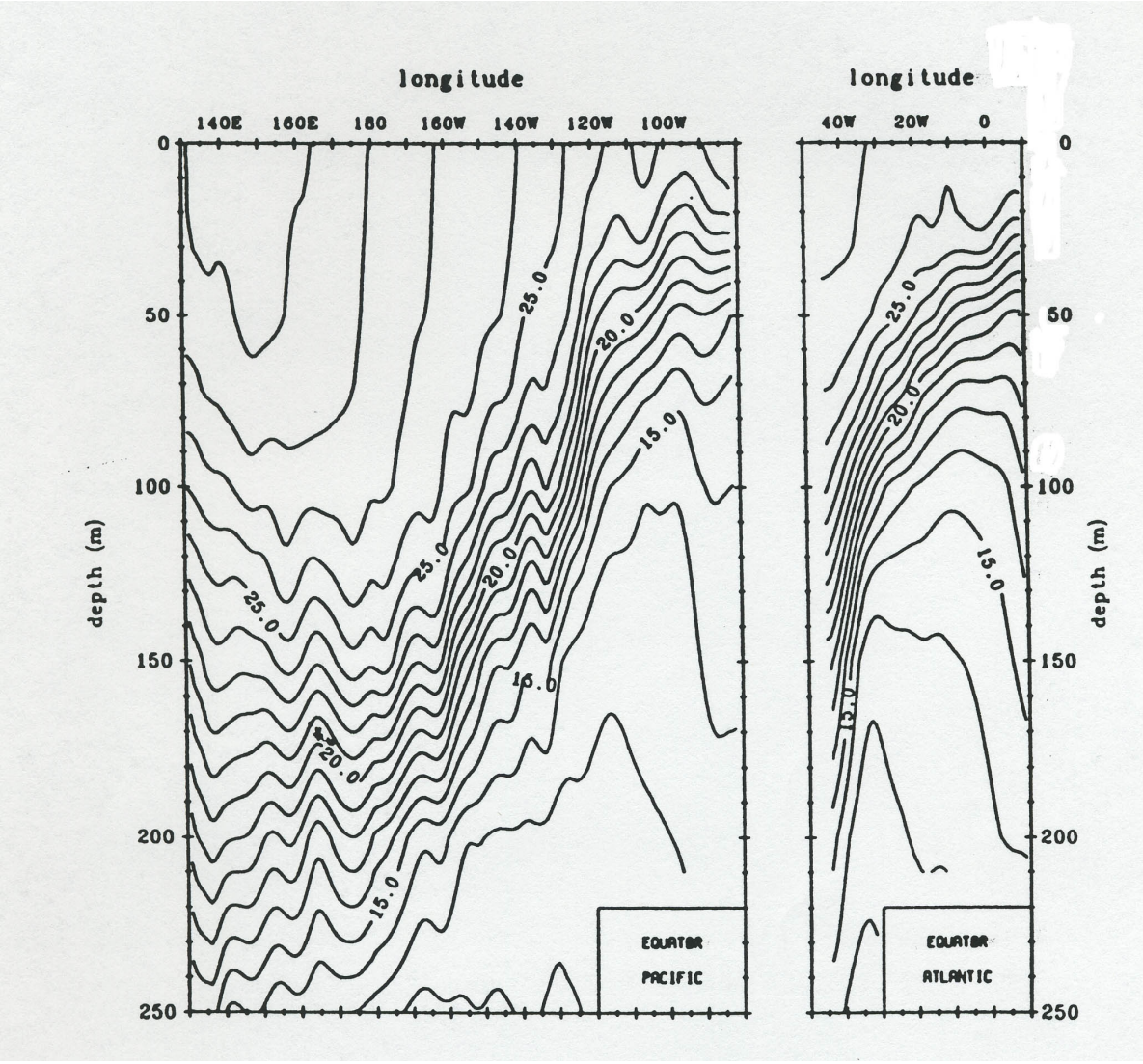

Figure 6: Upper-ocean, equatorial, zonal sections of T in the Atlantic and Pacific (from an unknown source).

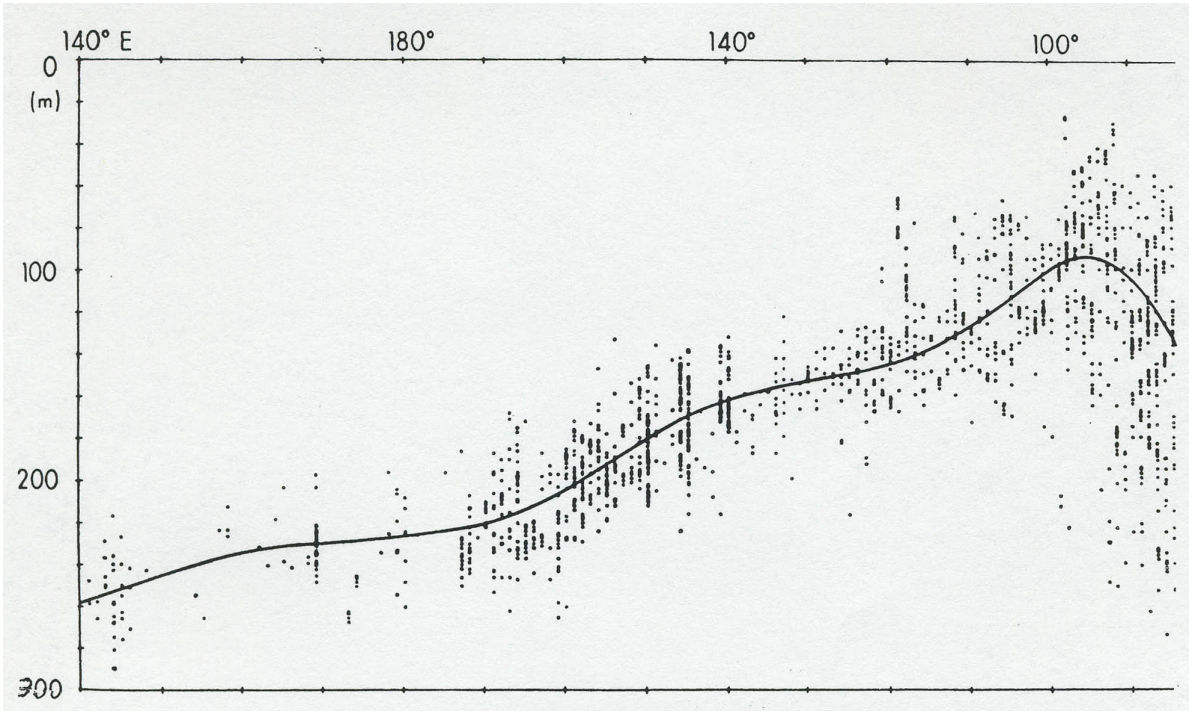

Figure 7: Depth of the 14^o isotherm in an upper-ocean, equatorial, zonal section in the Pacific, whose scatter is shown by dots (Meyers, 1979).

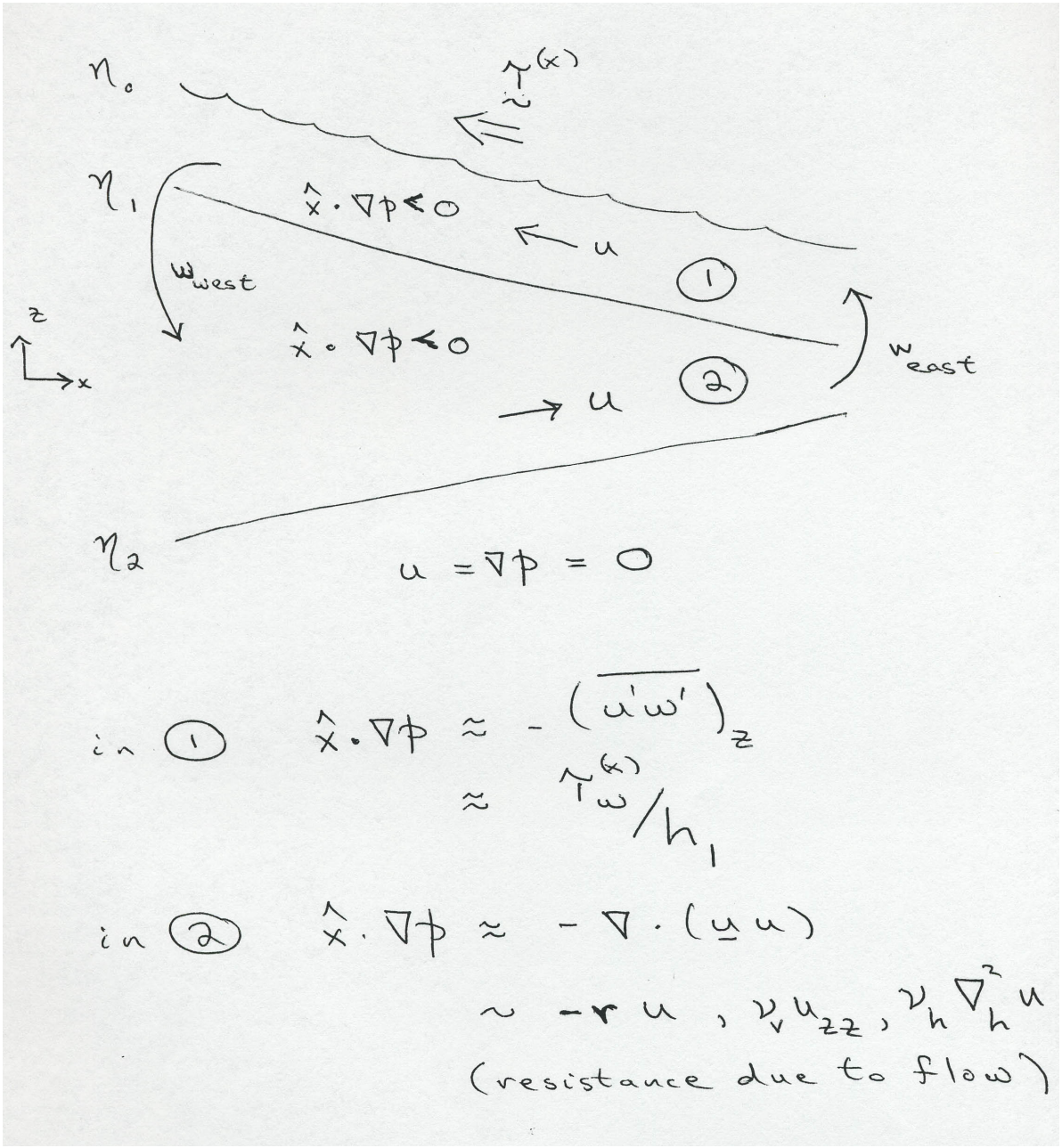

Figure 8: Schema of zonal momentum balance in the upper-ocean, equatorial, zonal plane.

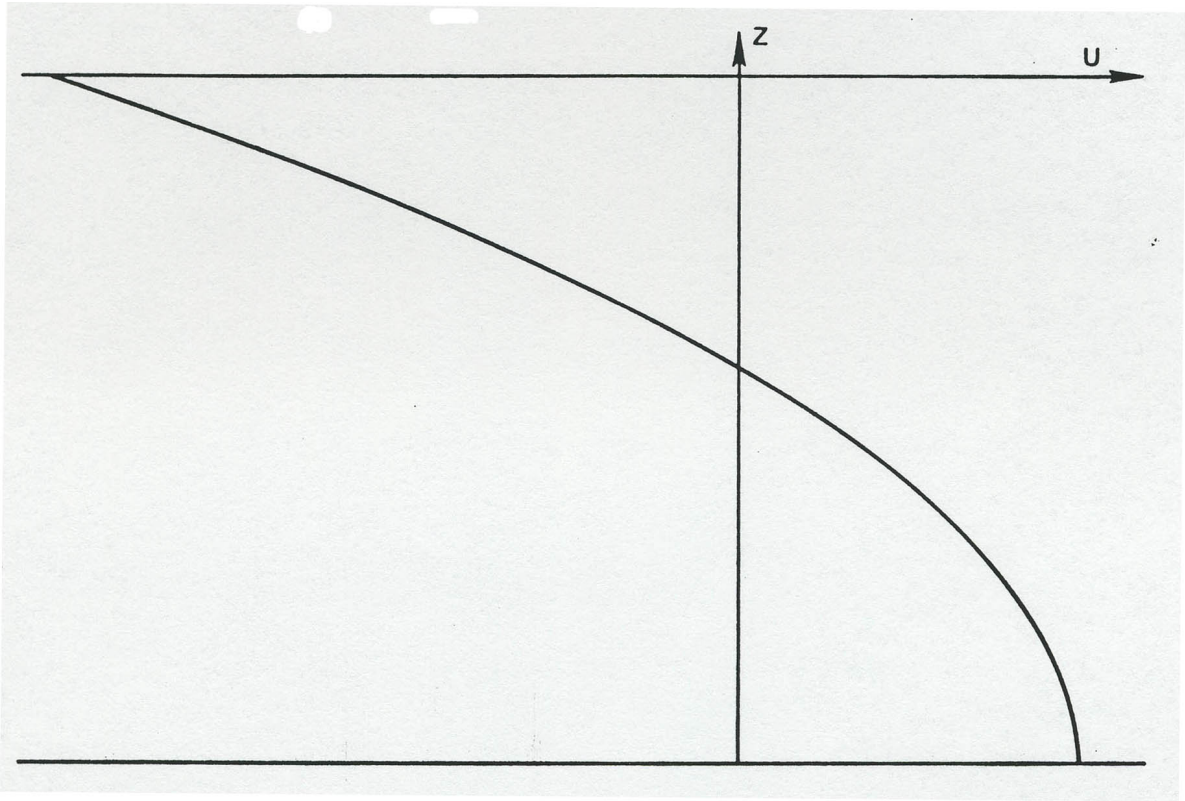

Figure 9: Vertical profile of eastward velocity at the equator obtained from eq. (2).

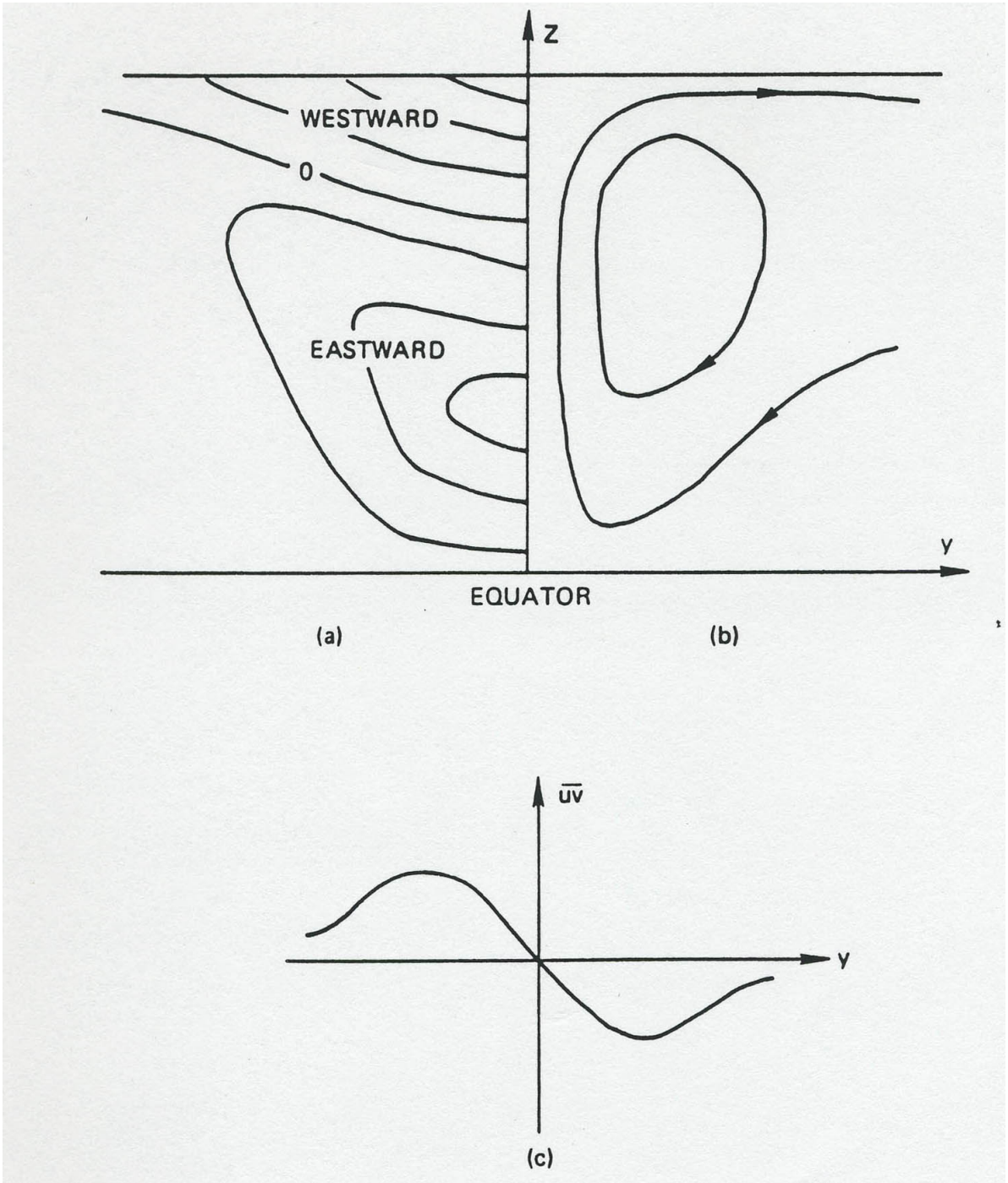

Figure 10: Typical variations of zonal velocity u (upper left), MOC (v, w) (upper right), and horizontal Reynolds uv for a linear, steady-state equatorial model with a westward wind.

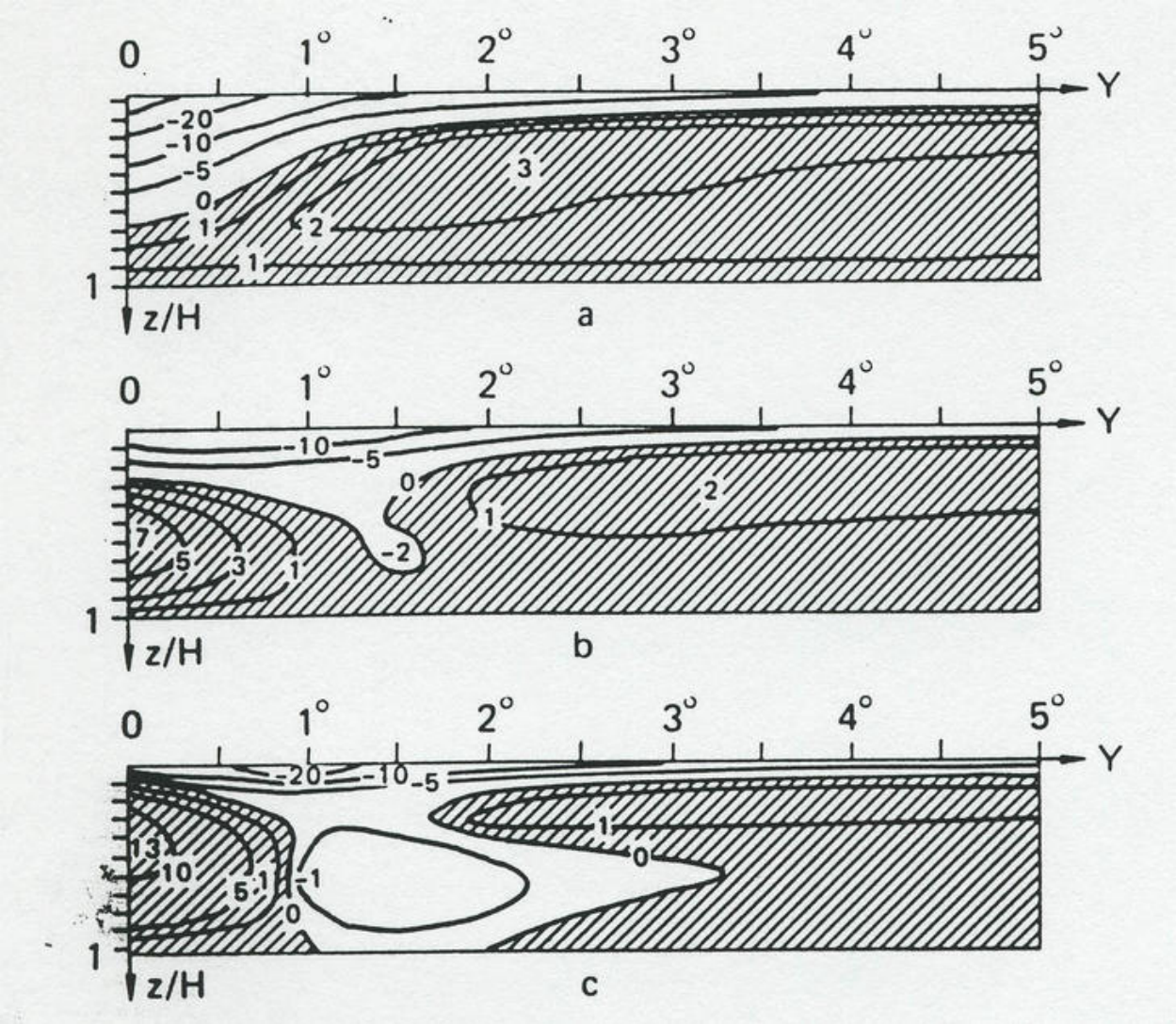

Figure 11: Structure of $u(y, z)$ for a nonlinear model with an eddy viscosity ν and westward wind stress (Mikhailova et al., 1967; Gill, 1975). The top panel is a linear solution, and the bottom two panels show increasingly nonlinear solutions. Only the northern half plane is shown.

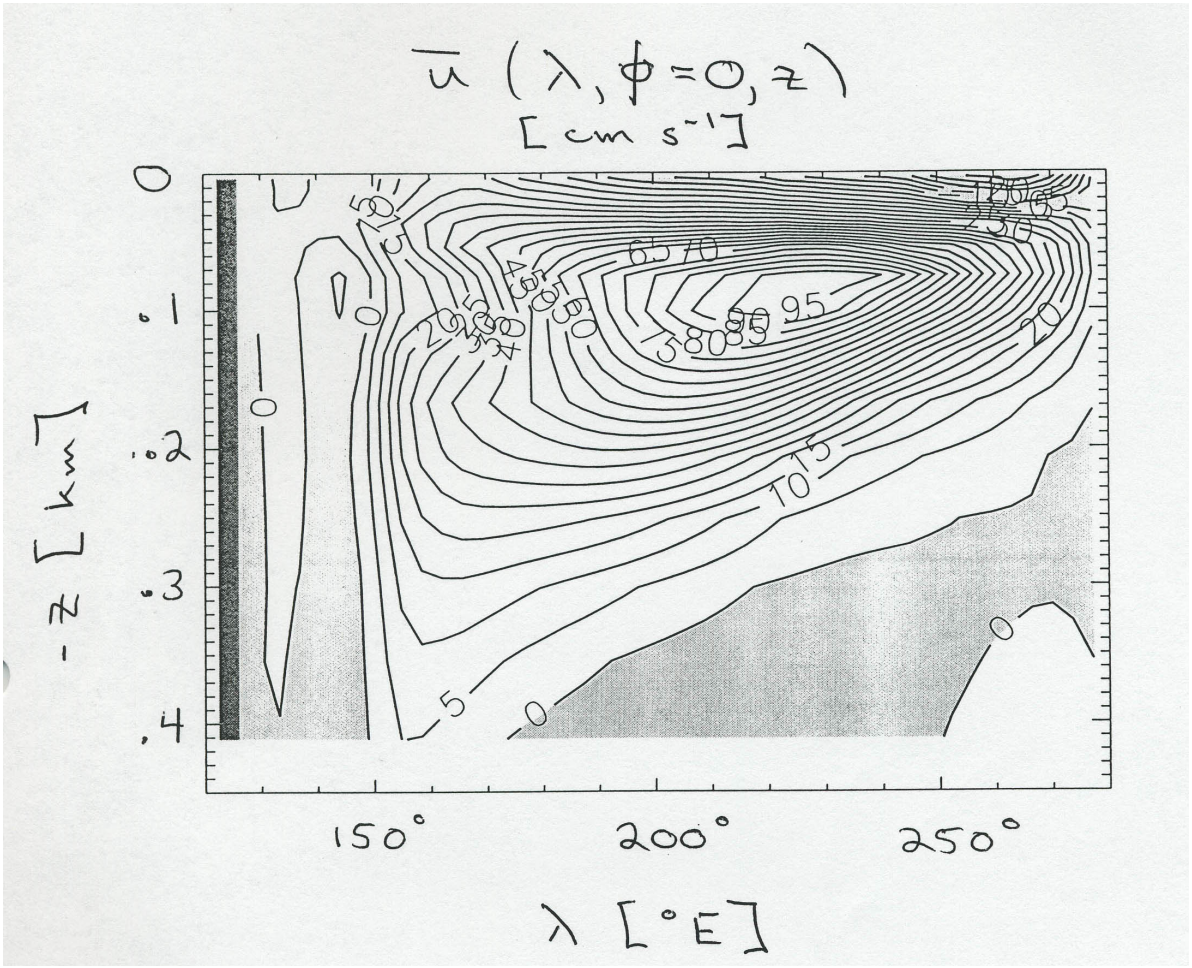

Figure 12: Zonal current in a Pacific equatorial plane from a GCM solution (Danabasoglu and McWilliams, 2000).

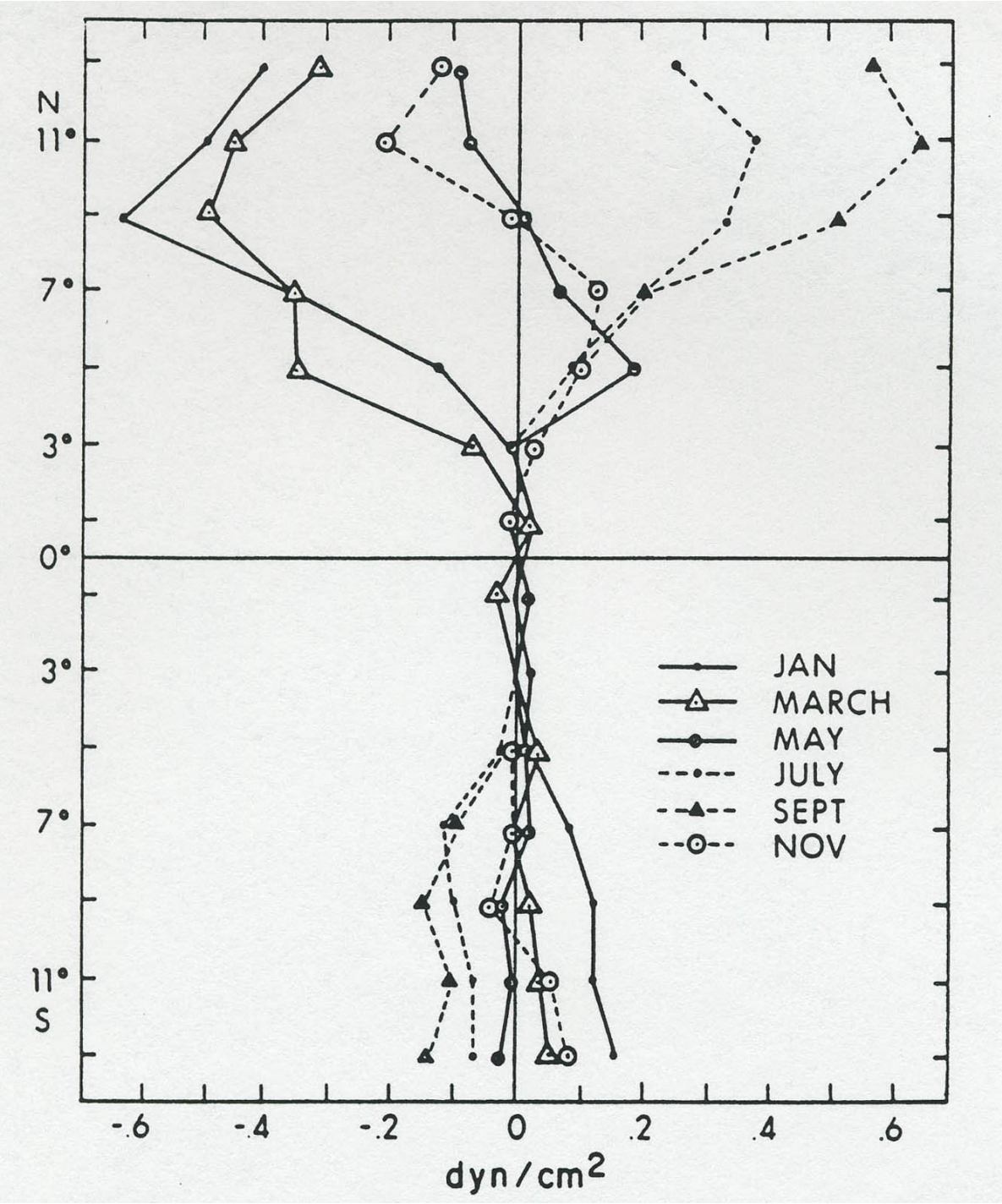

Figure 13: Annual cycle of zonal winds near the equator in the Pacific (Leetma et al., 1981).

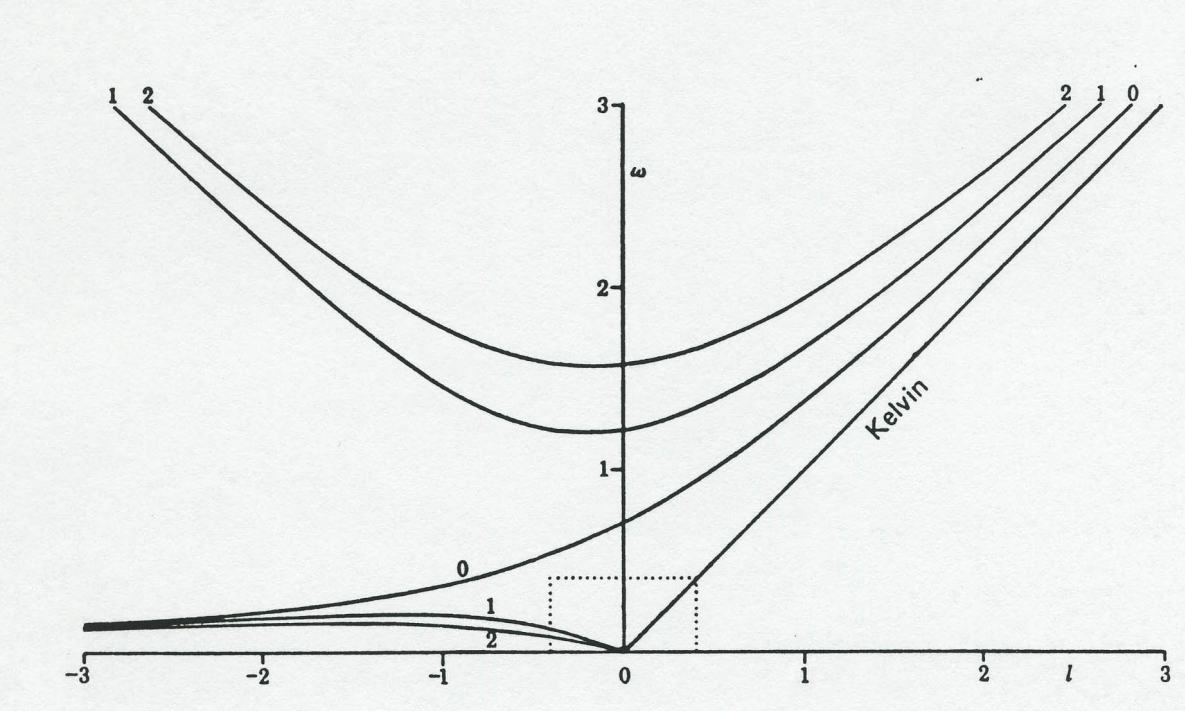

Figure 14: Nondimensional dispersion curves for the equatorial β-plane. ω is the eigenfrequency, and ℓ is the zonal wavenumber (Gill, 1975).

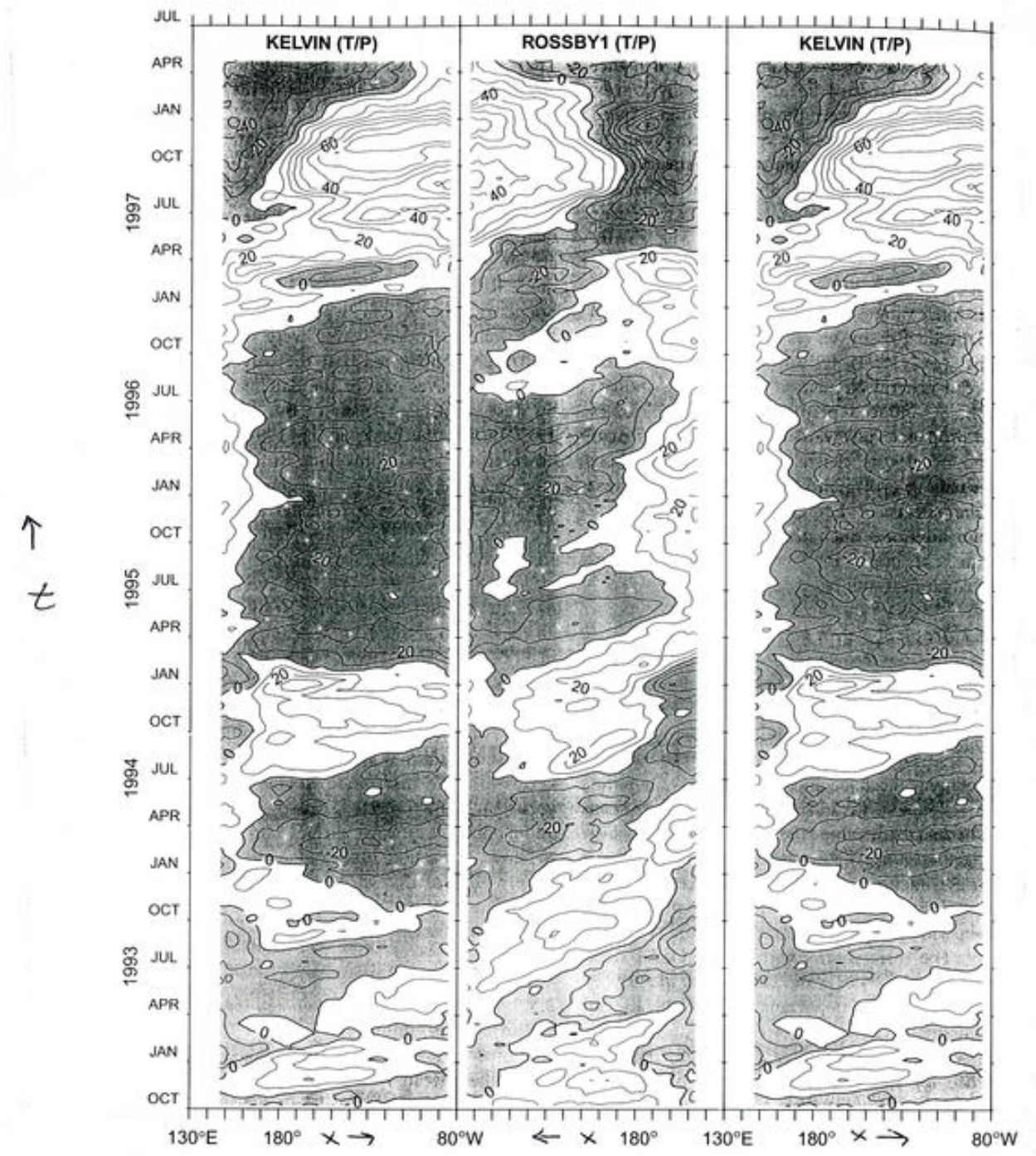

Figure 15: Longitude-time sections (a.k.a. Hovmüller diagrams) for the projections of altimetric sea level measurements onto Kelvin waves (left panel and repeated on the right for visualizing wave reflections at the western boundary) and first-meridional-mode Rossby waves (center panel, with longitude reversed for visualizing wave reflections at the eastern boundary) (Boulanger and Menkes, 1999). The units are arbitrary (!) and negative anomalies are shaded.

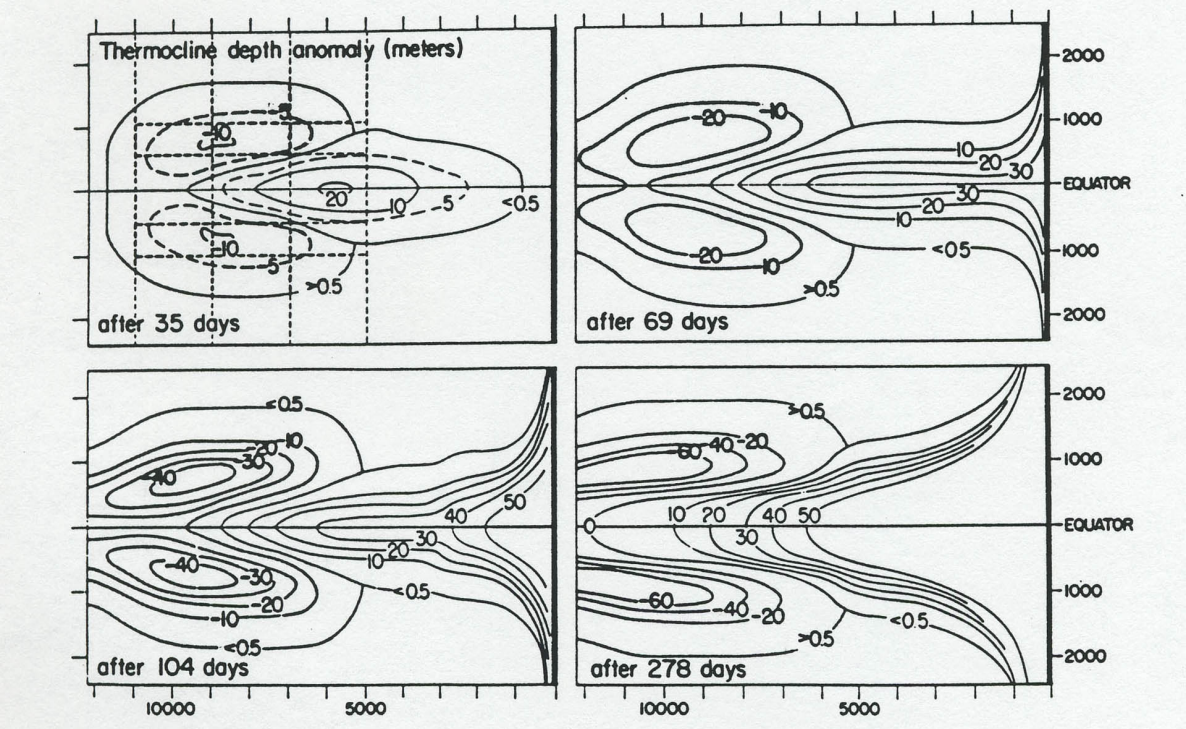

Figure 16: Transient development of a thermocline depth anomaly in response to a local, impulsive, eastward wind stress acting within the dashed lines in the first panel (McCreary, 1978). Notice the eastward Kelvin wave of thermocline elevation and the westward Rossby wave of thermocline depression. After the equatorial Kelvin wave reaches the eastern boundary, it is partly transformed into poleward propagating boundary Kelvin waves.

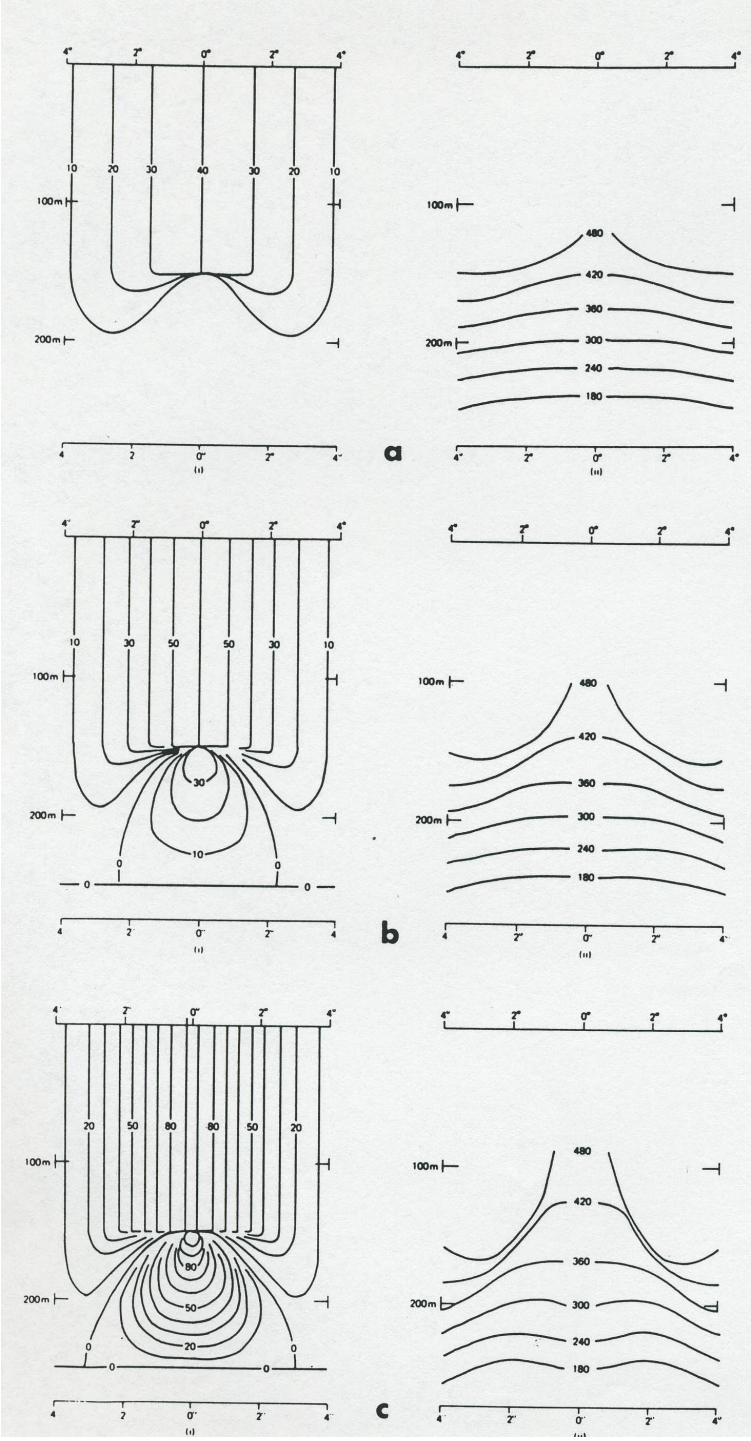

Figure 17: Transient development of u (left column) and dynamic height (right column) in response to a spatially uniform, impulsive westward wind stress acting on an initially resting, stratified ocean (Gill, 1975). These panels are for a meridional plane (y, z), and the successive rows are for successive times. Notice the spin up of the EUC and EC and the lifting of the pycnocline above the EUC's core.

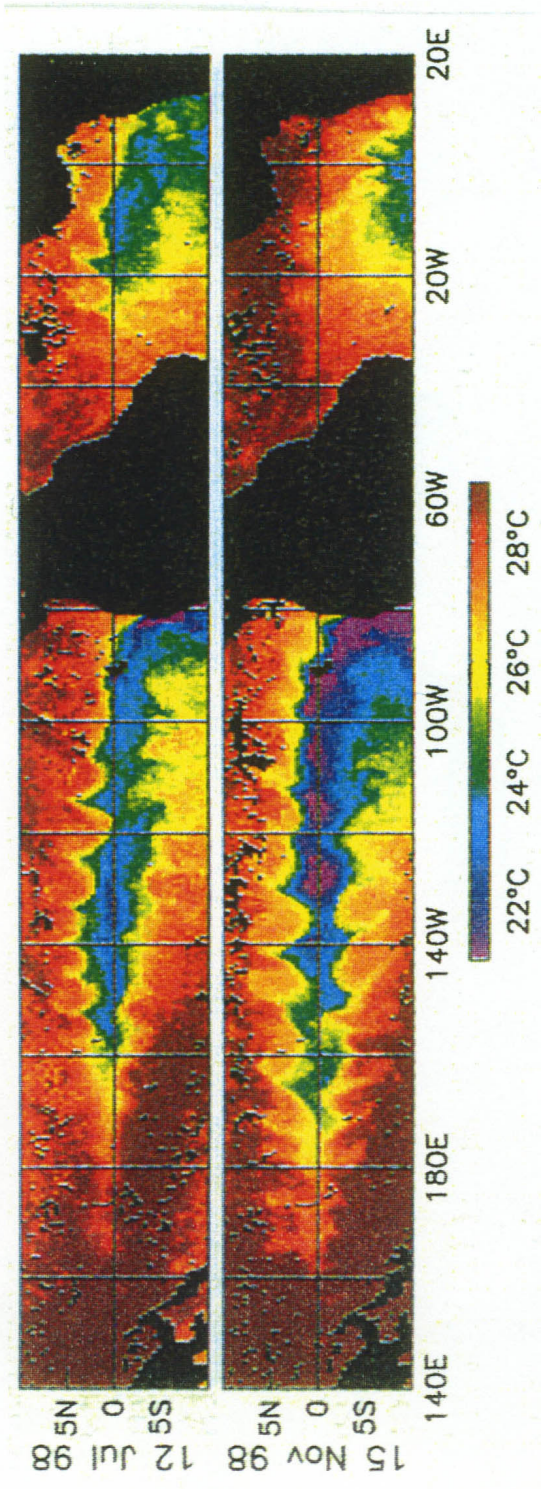

Figure 18: Selected 3-day composite-average maps of tropical SST measured from a satellite (Chelton et al., 2000). The cusps are TIW crests made visible at the boundary of the eastern equatorial "cold tongue" and the surrounding warmer water.

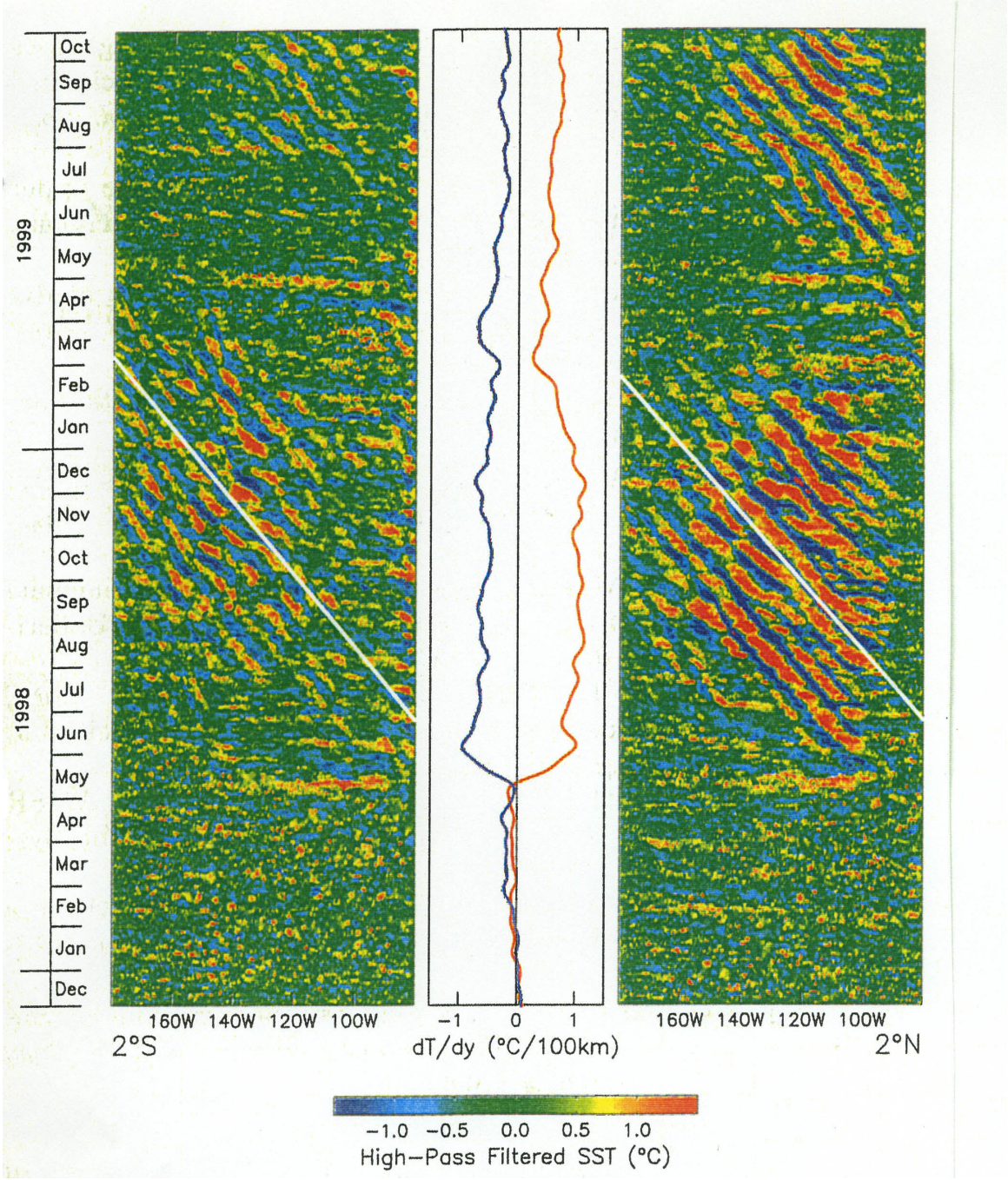

Figure 19: Time-longitude plots of 50-day high-pass filtered, tropical SST along 2^o S (left) and 2^o N (right), showing westward propgation, partial cross-equatorial correlation, and episodic occurrence (mainly during the northern fall season) (Chelton et al., 2000).

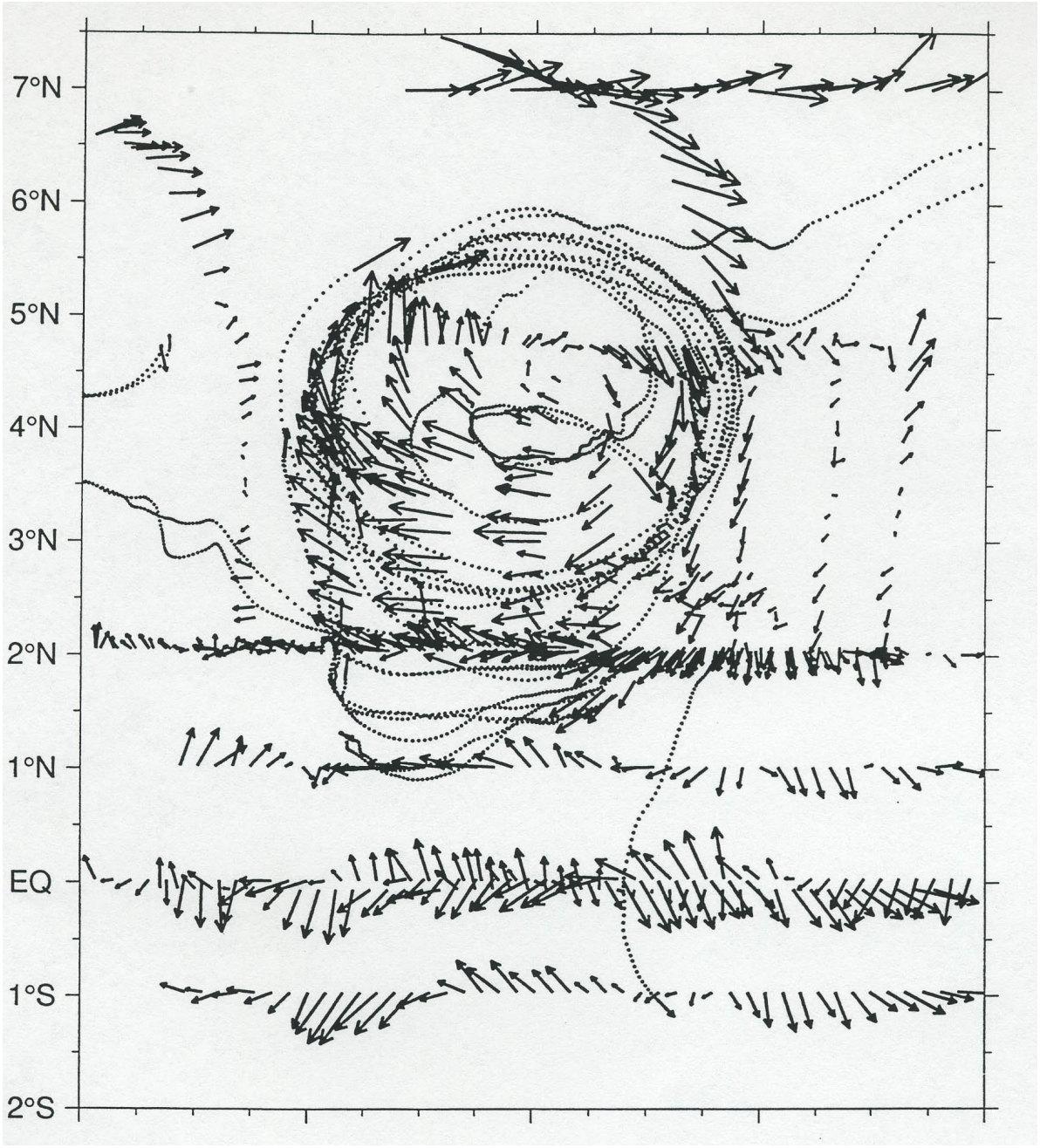

Figure 20: Velocity mapping of a TIW vortex in a horizontal-plane translating westward at 0.3 ms^{-1} (Kennan and Flament, 2000).

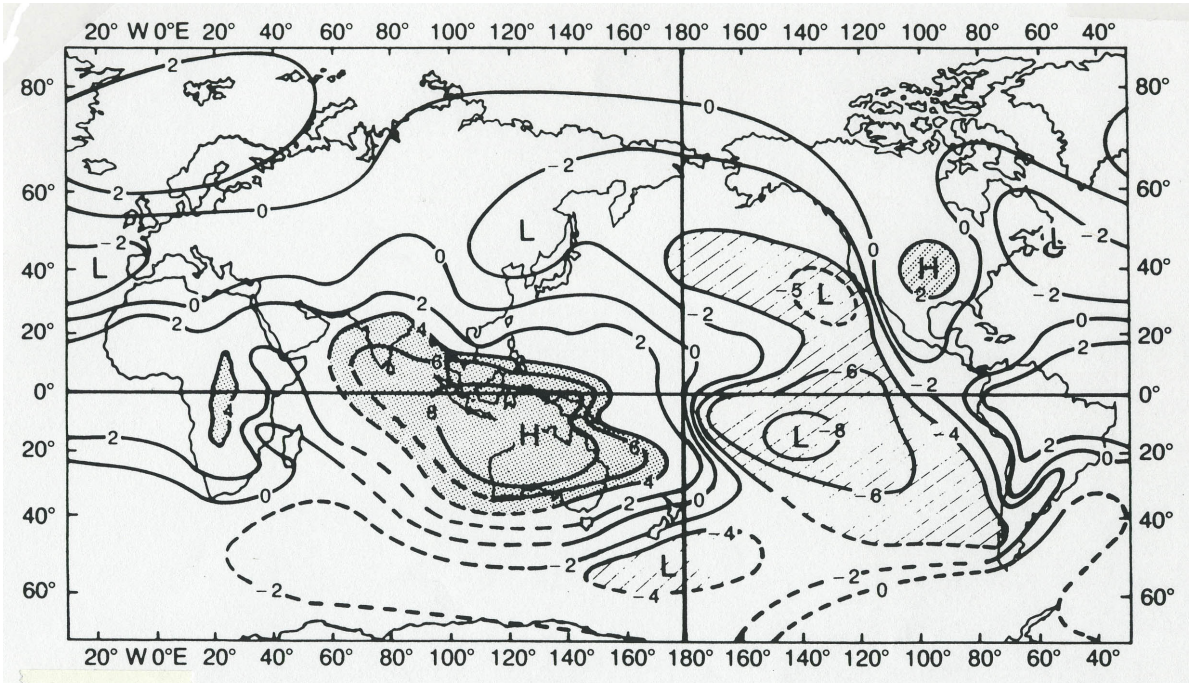

Figure 21: Correlation pattern of sea-level pressure with Darwin, Australia (Philander, 1990).

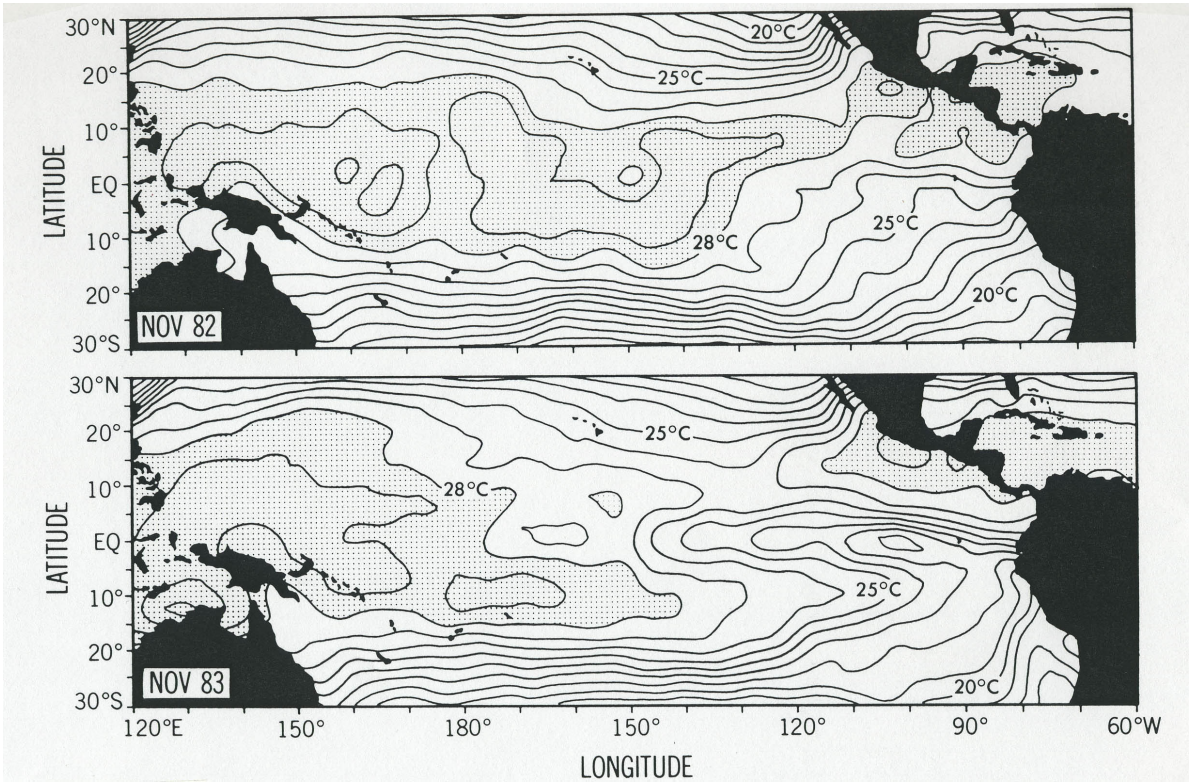

Figure 22: SST in 1982 (El Niño) and 1983 (La Niña) (Philander, 1990)

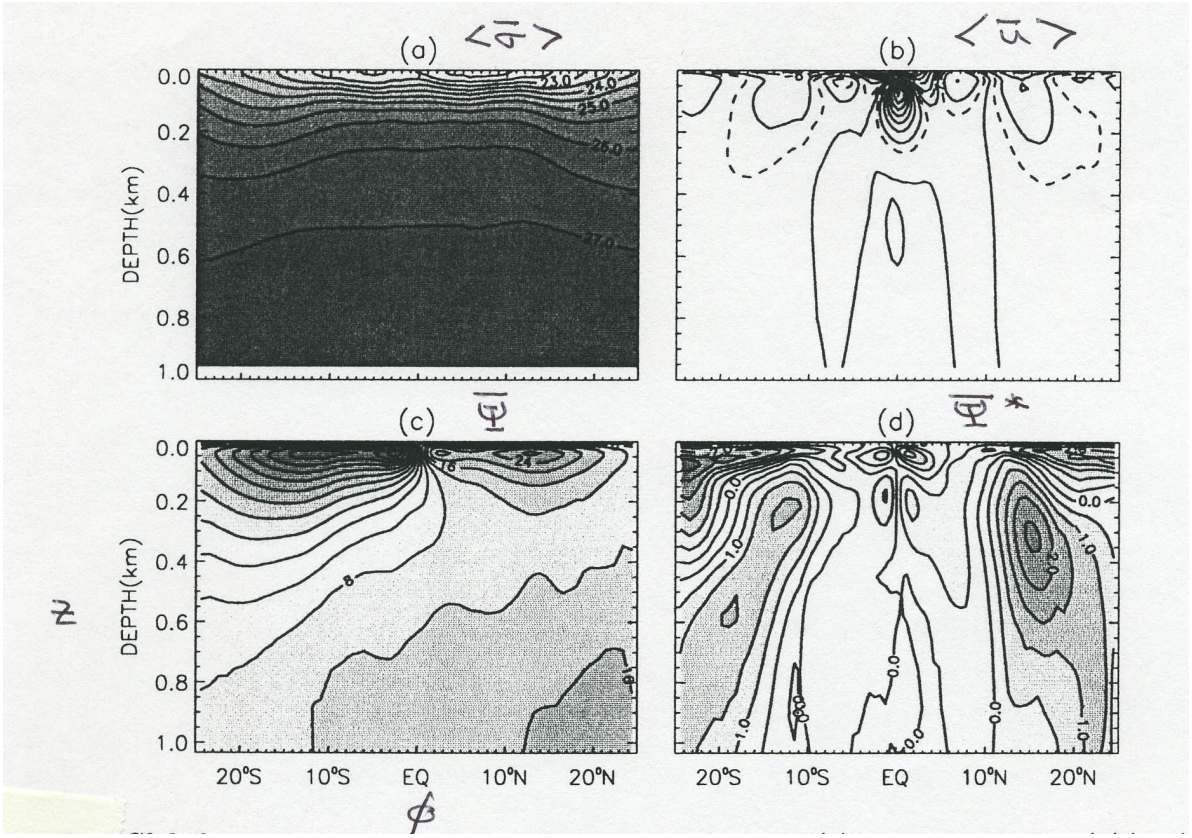

Figure 23: Global, upper-ocean, zonal- and time-mean quantities: (a) potential density, $\langle \overline{\sigma} \rangle (\phi, z)$ [CI = 0.5 kg m^{-3}] (with a surface reference pressure); (b) zonal velocity, $\langle \overline{u} \rangle (\phi, z)$ [CI = 0.04 m s^{-1}, with dashed lines for ± 0.02 m s^{-1}]; (c) Eulerian meridional overturning streamfunction, $\overline{\Psi}(\phi, z)$ [CI = 4 Sv]; (d) eddy-induced meridional overturning streamfunction, $\overline{\Psi}^*(\phi, z)$ [CI = 0.5 Sv] (McWilliams and Danabasoglu, 2001).

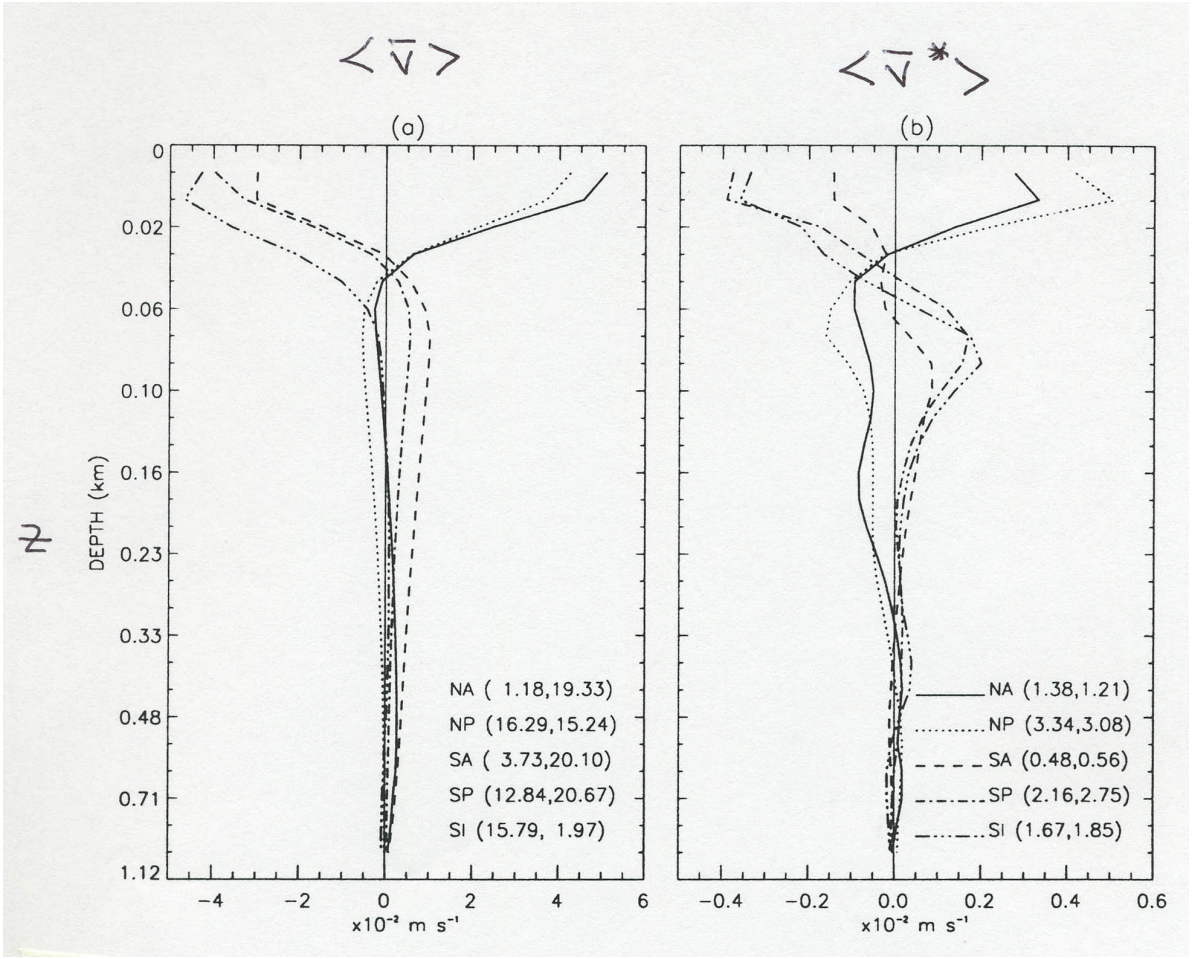

Figure 24: Meridional velocity, averaged temporally, zonally, and between 15-20° latitude, for each of the 5 tropical basins: (a) Eulerian, $\langle \overline{v} \rangle (z)$ [m s^{-1}], and (b) eddy-induced, $\langle \overline{v}^* \rangle (z)$ [m s^{-1}]. The insets list basin labels and total southward and northward transports [Sv] in the upper ocean (McWilliams and Danabasoglu, 2001).

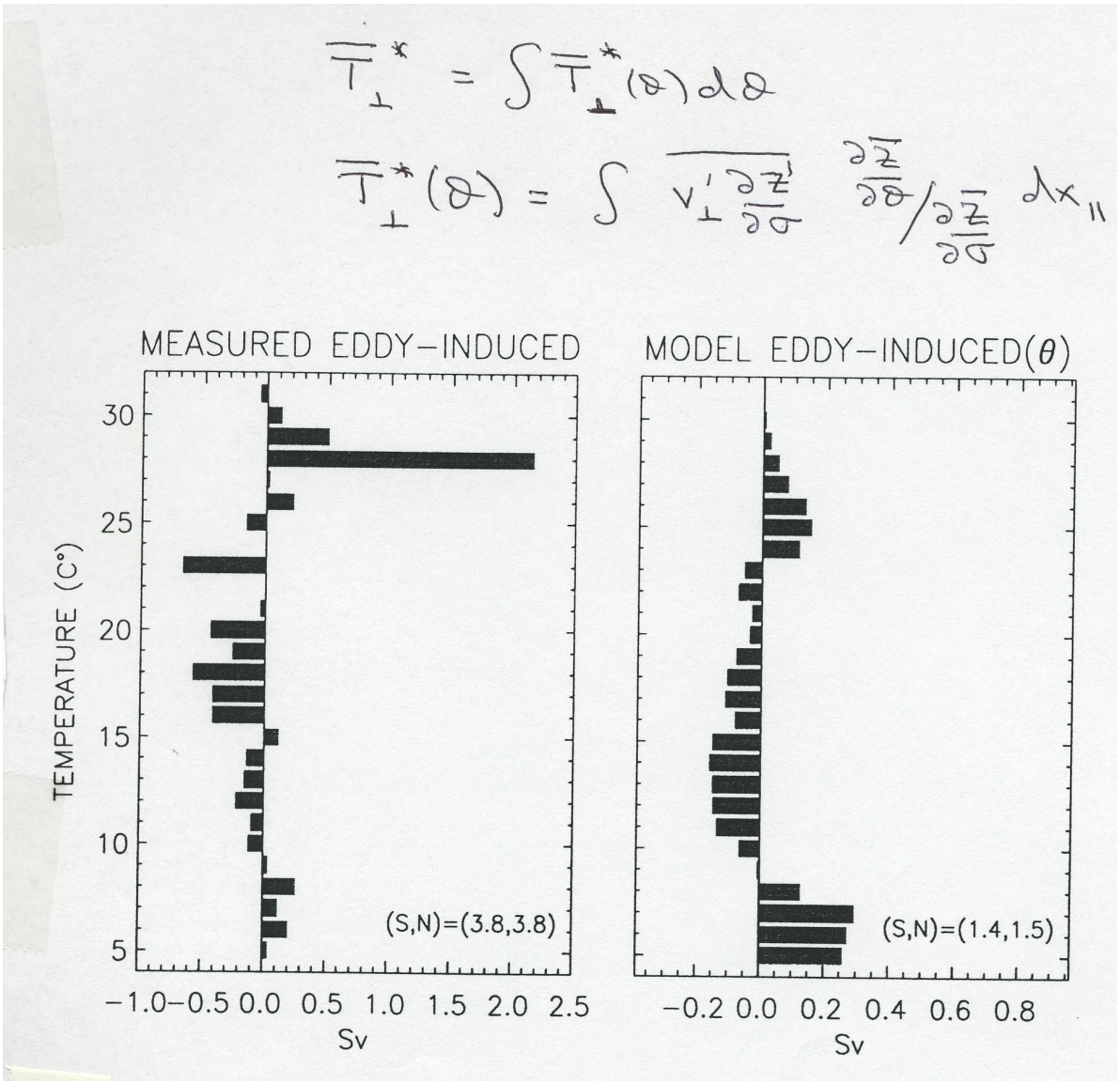

Figure 25: Eddy-induced normal heat transport, $\overline{T}^*_\perp(\theta)$ [Sv], in temperature bins ($\delta\theta = 1^\circ$ C), in the upper ocean ($\theta \geq 5^\circ$ C), averaged in time (8 years) and integrated along the repeated-hydrography line in the tropical North Pacific: (a) measured (Roemmich & Gilson, 2001); (b) modeled. Numerical labels indicate total southward and northward transports. Note the rescaled abscissa between (a) and (b), by a factor of 2.6. This is the ratio of their total southward and northward transports (McWilliams and Danabasoglu, 2001).

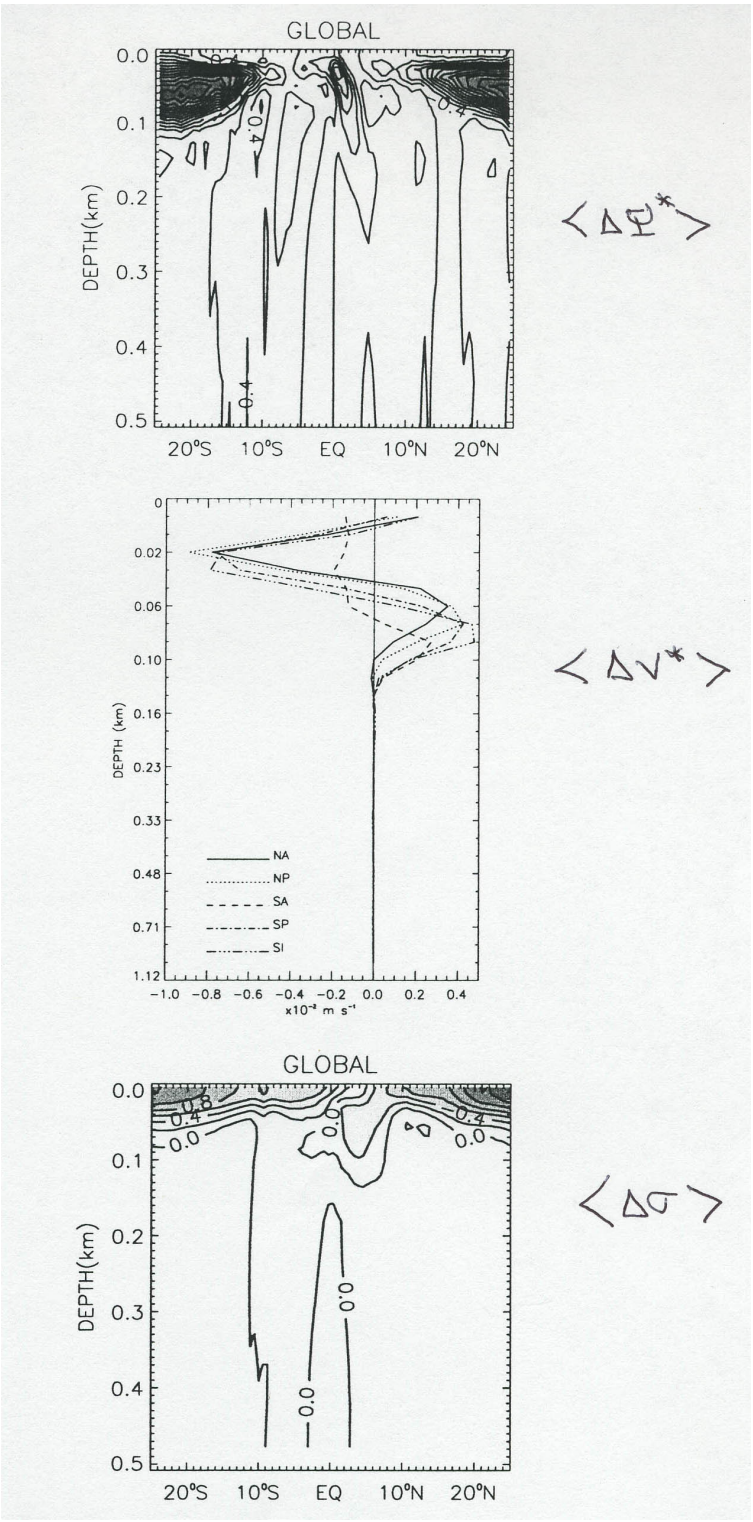

Figure 26: Mean-seasonal extreme differences (*i.e.,* the mean of the months ASO minus that of FMA): (a) global, $\Delta\Psi^*(\phi, z)$ [CI = 0.4 Sv]; (b) $\langle\Delta v^*\rangle(z)$ [m s^{-1}], averaged between 15-20°, with a stretched depth scale; and (c) global, $\langle\Delta\sigma\rangle(\phi, z)$ [CI = 0.2 kg m^{-3}] (McWilliams and Danabasoglu, 2001).

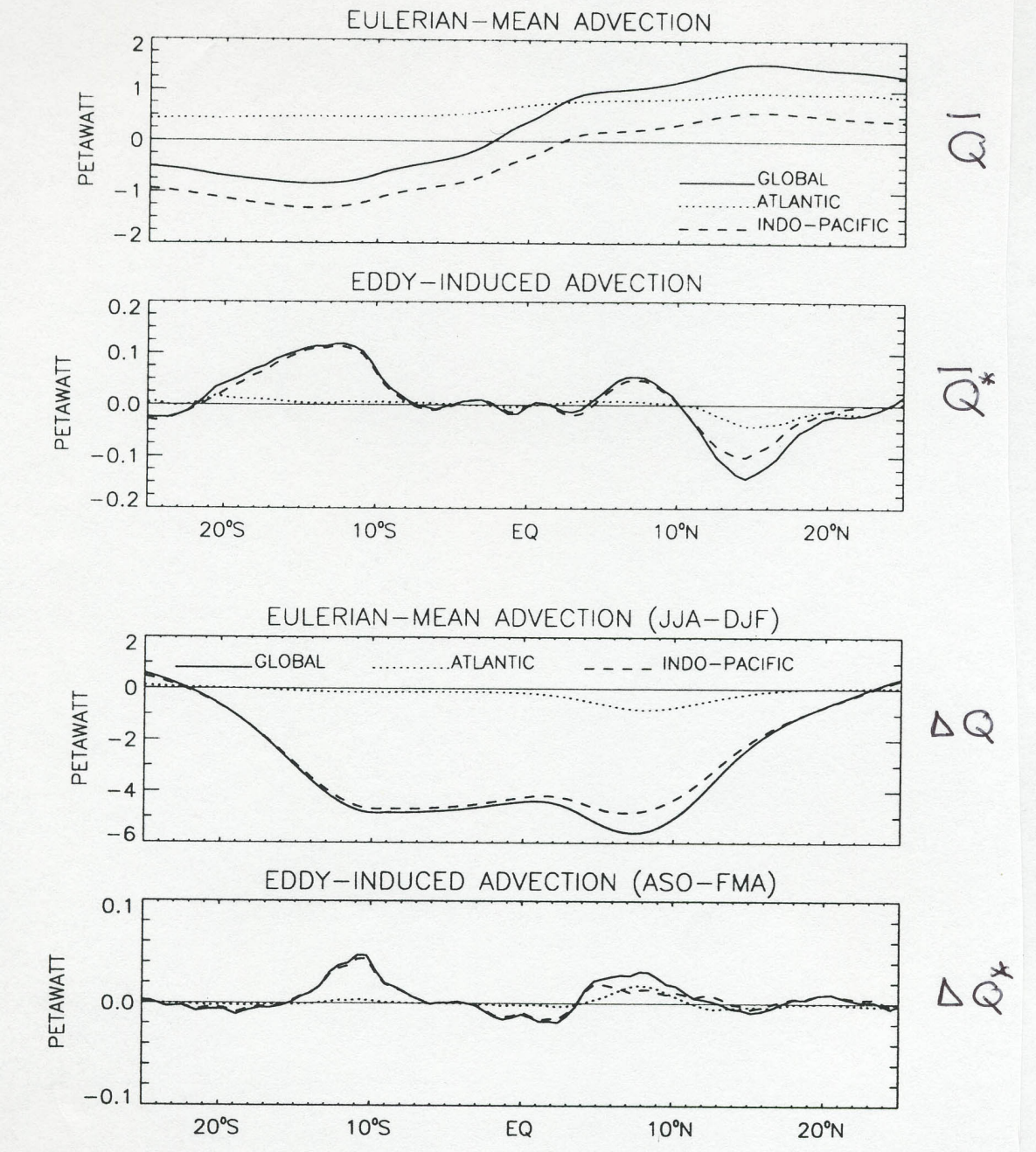

Figure 27: Vertically and zonally integrated meridional heat flux [PW]: time-mean, $\overline{Q}(\phi)$, (a) Eulerian and (b) eddy-induced components; and mean-seasonal extreme difference, $\Delta Q(\phi)$, (c) Eulerian (DJF minus JJA) and (d) eddy-induced (ASO minus FMA) (McWilliams and Danabasoglu, 2001).

References

Bauer, S., M. Swenson, A. Griffa, A. Mariano, and K. Owens, 1998: Eddy-mean flow decomposition and eddy-diffusivity estimates in the tropical Pacific Ocean: 1. Methodology. *J. Geophys. Res.*, **103**, 30855–30871.

Boulanger, J. and C. Menkes, 1999: Long equatorial wave reflection in the Pacific Ocean from TOPEX/POSEIDON data during the 1992-1998 period. *Clim. Dyn.*, **15**, 205–225.

Chelton, D., F. Wentz, C. Gentemann, R. de Szoeke, and M. Schlax, 2000: Satellite microwave SST observations of transequatorial tropical instability waves. *Geophys. Res. Lett.*, **27**, 1239–1242.

Danabasoglu, G. and J. McWilliams, 2000: An upper-ocean model for short-term climate variability. *J. Clim.*, **13**, 3380–3411.

d'Orgeville, M., B. Hua, and H. Sasaki, 2006: Equatorial deep jets triggered by a large vertical scale variability within the western boundary layer. *J. Mar. Res.*, in press.

Firing, E., 1987: Deep zonal currents in the central equatorial Pacific. *J. Mar. Res.*, **45**, 791–812.

Gent, P. and J. McWilliams, 1990: Isopycnal mixing in ocean circulation models. *J. Phys. Ocean.*, **20**, 150–155.

Gill, A., 1975: Models of equatorial currents. *Numerical Models of Ocean Circulation*, R. Reid, ed., Nat. Acad. Sci. Press, 181–203.

Hua, B., D. Moore, and S. Le Gentil, 1997: Inertial nonlinear equilibration of equatorial flows. *J. Fluid Mech.*, **331**, 345–371.

Kennan, S. and P. Flament, 2000: Observations of a tropical instability vortex. *J. Phys. Ocean.*, **30**, 2277–2301.

Knauss, J., 1960: Measurements of the Cromwell Current. *Deep Sea Res.*, **6**, 265–286.

Krauss, W. and C. Böning, 1987: Lagrangian properties of eddy fields in the northern North Atlantic as deduced from satellite-tracked buoys. *J. Mar. Res.*, **45**, 259–291.

Leetma, A., J. McCreary, and D. Moore, 1981: Equatorial currents: Observations and theory. *Evolution of Physical Oceanography*, B. Warren and C. Wunsch, eds., MIT Press, 184–196.

Lemasson, L. and B. Piton, 1968: *Cah. ORSTOM, Ser. Oceanogr.*, **6**, 39–46.

Mayer, D. and R. Weisberg, 1993: A description of COADS surface meteorological fields and the implied Sverdrup transports for the Atlantic Ocean from 30S to 60N. *J. Phys. Ocean.*, **23**, 2201–2221.

McCreary, J., 1978: Eastern ocean response to changing wind systems. *Review Papers of Equatorial Oceanography—FINE Workshop Proceedings*, **Nova University**, 1–22.

McWilliams, J. and G. Danabasoglu, 2001: Eulerian and eddy-induced meridional overturning circulations in the tropics. *J. Phys. Ocean.*, **32**, 2054–2071.

McWilliams, J., G. Danabasoglu, and P. Gent, 1996: Tracer budgets in the warm water sphere. *Ann. Rev. Fluid. Mech.*, **28**, 1–34.

Meyers, G., 1979: Annual variation of the slope of the 14 C isotherm along the equator in the Pacific Ocean. *J. Phys. Ocean.*, **9**, 885–891.

Mikhailova, E., A. Felsenbaum, and N. Shapiro, 1967: A contribution to the nonlinear theory of currents at the equator. *Dokl. Akad. Nauk. USSR*, **175**, 574–577.

Neelin, J., D. Battisti, A. Hirst, F.-F. Jin, Y. Wakata, T. Yamagata, and S. Zebiak, 1998: Enso theory. *J. Geophys. Res.*, **7**, 14261–14290.

Pedlosky, J., 1987: An inertial theory of the equatorial undercurrent. *J. Phys. Ocean.*, **17**, 1978–1985.

Philander, S., 1990: *El Nino, La Nina, and the Southern Oscillation*. Academic Press, 289 pp.

Roemmich, D. and J. Gilson, 2001: Eddy transport of heat and thermocline waters in the North Pacific: A key to interannual/decadal climate variability? *J. Phys. Ocean.*, **31**, 675–688.

Sturm, M. and K. Voigt, 1966: Observations of the structure of the equatorial undercurrent in the Gulf of Guinea in 1964. *J. Geophys. Res.*, **71**, 3105–3108.

Sundermeyer, M. and J. Price, 1998: Lateral mixing and the North Atlantic Tracer Release Experiment: Observations and numerical simulations of Lagrangian particles and a passive tracer. *J. Geophys. Res.*, **103**, 21481–21497.

Taft, B., 1967: Equatorial undercurrent of the Indian Ocean. *Sud. Trop. Ocean, U. Miami*, **5**, 3–14.

Wüst, G., 1949: über die Zweiteilung der Hydrosphäre. *Dt. hydrogr. Z.*, **2**, 218–225.